An asymptotic-preserving scheme for Euler equations I: non-ideal gases

Giuseppe Orlando, Luca Bonaventura

An asymptotic-preserving scheme for Euler equations I: non-ideal gases

Giuseppe Orlando[(1)], Luca Bonaventura[(2)]

[(1)] CMAP, CNRS, École Polyechnique, Institute Polytechnique de Paris
Route de Saclay, 91120 Palaiseau, France
giuseppe.orlando@polytechnique.edu

[(2)] Dipartimento di Matematica, Politecnico di Milano
Piazza Leonardo da Vinci 32, 20133 Milano, Italy
luca.bonaventura@polimi.it

Keywords: Asymptotic-preserving, all Mach, Euler equations, IMEX, Discontinuous Galerkin, Non-ideal gas.

Abstract

We analyze a general Implicit-Explicit (IMEX) time discretization for the compressible Euler equations of gas dynamics, showing that they are asymptotic-preserving (AP) in the low Mach number limit. The analysis is carried out for a general equation of state (EOS). We consider both a single asymptotic length scale and two length scales. We then show that, when coupling these time discretizations with a Discontinuous Galerkin (DG) space discretization with appropriate fluxes, an all Mach number numerical method is obtained. A number of relevant benchmarks for ideal gases and their non-trivial extension to non-ideal EOS validate the performed analysis.

1 Introduction

The compressible Euler equations of gas dynamics are the standard mathematical model in several applications such as atmosphere dynamics [51], combustion or astrophysics. For these equations, one can consider two opposite regimes: one in which the flow is strongly subsonic, and therefore acoustic waves are much faster than the local fluid velocity, and the other in which the fluid moves at high speed and compressibility plays a key role. The relevant non-dimensional number which identifies the regime is the local Mach number M_{loc}, defined as $M_{loc} = \frac{|\mathbf{u}|}{c}$, where $|\mathbf{u}|$ is the magnitude of the local fluid velocity and c is the speed of sound. When the Mach number tends to zero, under suitable conditions, the compressible Euler equations converge to the incompressible Euler equations, see [21, 37], and the references therein for the analysis of singular limits of compressible flows. Weakly compressible flows are an example of problem with multiple length and time scales. Hence, the design of efficient and stable numerical schemes for such models is a challenging task and typically requires specific numerical treatments. For this purpose, the concept of asymptotic-preserving (AP) schemes has been introduced, see e.g. [28]. Consider a continuous physical model $\mathcal{M}^\varepsilon$ which involves a perturbation parameter ε, where in general $\varepsilon \ll 1$. Denote by $\mathcal{M}^0$ the limit of $\mathcal{M}^\varepsilon$ when $\varepsilon \to 0$, e.g. the incompressible Euler equations in our framework. Let now $\mathcal{M}^\varepsilon_{\Delta t}$ be a time discretization method which provides a consistent discretization of $\mathcal{M}^\epsilon$. The scheme $\mathcal{M}^\varepsilon_{\Delta t}$ is said to be asymptotic-preserving (AP) if its stability condition is independent of ε and if its limit $\mathcal{M}^\varepsilon_{\Delta t}$ for $\varepsilon \to 0$ provides a consistent discretization of the continuous limit model $\mathcal{M}^0$. We analyze here the Euler equations of gas dynamics and the parameter ε is represented by the Mach number M, as defined in Section 2. Since the seminal contribution [38], several AP schemes for Euler equations have been proposed in the literature, see among many others [1, 7, 13, 16, 17, 40, 41, 44, 56] and the references therein. While a complete review of all the different approaches for low Mach flows is out of the scope of the present work, we briefly outline some of the strategies proposed in the literature to deal with low Mach flows, in order to highlight the main differences with the proposed numerical method. Following the discussion in [38], a class of AP methods [13, 14] proposes to decouple acoustic and transport phenomenon, leading to the so-called Lagrange-Projection like schemes. Hence, an operator splitting is applied, solving first the transport subsystem and dealing with acoustic effects afterwards. Following again [38], another class of AP schemes [16, 44] considers a splitting of the fluxes into non-stiff and stiff parts. More specifically, effects of global compression or long wave acoustics are considered explicitly and then an implicit pressure correction is applied. Another class of popular methods are the so-called pressure correction schemes. They extend the projection techniques widely used for incompressible flows [15, 49, 54] and, starting from [30, 31], several approaches have been proposed [32, 33, 55]. Finally, a Suliciu type relaxation scheme [52], splitting the pressure in a slow and a fast acoustic part, has been proposed in [56], whereas a Jin-Xin type relaxation method, building a linear hyperbolic relaxation system with a small dissipative correction to approximate the Euler equations, has been presented in [1].

We analyze here the AP properties of a general class of Implicit-Explicit (IMEX) time discretization schemes. The key observation is that, as first proposed in [12], it suffices to adopt an implicit treatment of the pressure gradient term within the

momentum equation and of the pressure work term in the energy equation to remove the acoustic CFL restriction and to decouple acoustic and transport effects (see also Appendix A). Similar approaches have been proposed e.g. in [7, 10]. Moreover, we consider a general equation of state (EOS), for which only a small number of studies have been devoted [1, 16]. We also extend the analysis performed in [38] for two length scales to the case of a general EOS. Notice that, several low Mach schemes have been proposed for a barotropic equation of state [8, 26, 34]. As discussed in [38], the assumption of a barotropic fluid, for which a direct relation between the pressure and the density exists, restricts the analysis to constant-entropy data and the limiting case is an incompressible flow with constant density. However, large amplitude density fluctuations are crucial for an accurate description of reacting flows [38], for atmospheric applications and for the analysis of relevant fluid dynamics instabilities, as we will see in Section 5. Finally, we show that an all Mach number numerical method can be obtained coupling these time discretizations with a Discontinuous Galerkin (DG) space discretization [23] with appropriate fluxes. The numerical verification is based on the IMEX-DG method proposed in [46, 47, 48], which represents a particular case of the IMEX time discretization analyzed in this work. More specifically, a second order IMEX Additive Runge Kutta (ARK) scheme [36] is employed.

The paper is structured as follows. In Section 2, we derive the limits of the continuous model considering both a single length scale and two length scales. In Section 3, we show the AP property of a general class of IMEX-ARK methods, whereas in Section 4 we discuss some details of the DG formulation that allows us to obtain a numerical scheme effective for all Mach numbers. In Section 5, some numerical results to verify the robustness of the proposed approach both for $M = O(1)$ and $M \ll 1$, using the numerical method developed in [46, 47, 48], are presented. Finally, some conclusions and perspectives for future work are discussed in Section 6.

2 Asymptotic analysis for the continuous model

We aim to investigate the limit of the fully compressible Euler equations of gas dynamics as the Mach number goes to zero. Let $\Omega \subset \mathbb{R}^d, 1 \leq d \leq 3$ be a connected open bounded set with a sufficiently smooth boundary $\partial\Omega$ and denote by $\mathbf{x}$ the spatial coordinates and by t the temporal coordinate. The mathematical model reads as follows:

$$\begin{aligned} \frac{\partial \rho}{\partial t} + \nabla\cdot(\rho\mathbf{u}) &= 0 \\ \frac{\partial \rho\mathbf{u}}{\partial t} + \nabla\cdot(\rho\mathbf{u}\otimes\mathbf{u}) + \nabla p &= \mathbf{0} \\ \frac{\partial \rho E}{\partial t} + \nabla\cdot[(\rho E + p)\,\mathbf{u}] &= 0. \end{aligned} \tag{1}$$

Here, ρ is the density, $\mathbf{u}$ is the fluid velocity, p is the pressure, and E is the total energy per unit of mass. The previous set of equations has to be completed by an equation od state (EOS). Notice that no external source terms, such as gravity terms, are considered in (1). The total energy ρE can be rewritten as $\rho E = \rho e + \rho k$, where e is the internal energy and $k = \frac{1}{2}|\mathbf{u}|^2$ is the kinetic energy. We also introduce the

specific enthalpy $h = e + \frac{p}{\rho}$ and we notice that one can rewrite the energy flux as

$$(\rho E + p)\,\mathbf{u} = \left(e + k + \frac{p}{\rho}\right)\rho\mathbf{u} = (h + k)\,\rho\mathbf{u}. \tag{2}$$

Hence, (1) can be rewritten as

$$\begin{aligned} \frac{\partial \rho}{\partial t} + \nabla\cdot(\rho\mathbf{u}) &= 0 \\ \frac{\partial \rho\mathbf{u}}{\partial t} + \nabla\cdot(\rho\mathbf{u}\otimes\mathbf{u}) + \nabla p &= \mathbf{0} \\ \frac{\partial \rho E}{\partial t} + \nabla\cdot[(h+k)\,\rho\mathbf{u}] &= 0. \end{aligned} \tag{3}$$

Introduce reference scaling values $\mathcal{T}, \mathcal{L}$, and $\mathcal{U}$ for time, length, and velocity, respectively. We also introduce reference values $\mathcal{P}$ for the pressure and $\mathcal{R}$ for the density. The Buckingham π theorem [9] states that there are $n - k$ relevant non-dimensional parameters that characterize the model, where n is the number of independent physical variables and k is the rank of the matrix which associates to each physical parameter its unit of measure. Hence, there are 2 non-dimensional parameters associated to (3). We assume that the internal energy scales as $\mathcal{I} \approx \frac{\mathcal{P}}{\mathcal{R}}$ and that the total energy scales as $\mathcal{E} \approx \mathcal{I} + \mathcal{U}^2$. Finally, we assume that the specific enthalpy scales as $\mathcal{H} \approx \mathcal{I} + \frac{\mathcal{P}}{\mathcal{R}}$. Introduce the following non-dimensional parameters

$$St = \frac{\mathcal{L}}{\mathcal{T}\mathcal{U}} \qquad M^2 = \frac{\mathcal{R}\mathcal{U}^2}{\mathcal{P}} \tag{4}$$

and notice that

$$\frac{\mathcal{I} + \frac{\mathcal{P}}{\mathcal{R}}}{\mathcal{E}} = \frac{2\frac{\mathcal{P}}{\mathcal{R}}}{\frac{\mathcal{P}}{\mathcal{R}} + \mathcal{U}^2} = \frac{\frac{2}{M^2}}{\frac{1}{M^2} + 1} = O(1) \tag{5}$$

$$\frac{U^2}{\mathcal{E}} = \frac{\mathcal{U}^2}{\frac{\mathcal{P}}{\mathcal{R}} + \mathcal{U}^2} = \frac{1}{1 + \frac{1}{M^2}} = O\left(M^2\right). \tag{6}$$

Hence, the non-dimensional version of (3) reads as follows:

$$\begin{aligned} St\frac{\partial \rho}{\partial t} + \nabla\cdot(\rho\mathbf{u}) &= 0 \\ St\frac{\partial \rho\mathbf{u}}{\partial t} + \nabla\cdot(\rho\mathbf{u}\otimes\mathbf{u}) + \frac{1}{M^2}\nabla p &= \mathbf{0} \\ St\frac{\partial \rho E}{\partial t} + \nabla\cdot\left[\left(h + kM^2\right)\rho\mathbf{u}\right] &= 0, \end{aligned} \tag{7}$$

where, with a slight abuse of notation, the non-dimensional variables are denoted with the same symbols of the dimensional ones. Finally, we assume that $St \approx 1$, so as to obtain

$$\begin{aligned} \frac{\partial \rho}{\partial t} + \nabla\cdot(\rho\mathbf{u}) &= 0 \\ \frac{\partial \rho\mathbf{u}}{\partial t} + \nabla\cdot(\rho\mathbf{u}\otimes\mathbf{u}) + \frac{1}{M^2}\nabla p &= \mathbf{0} \\ \frac{\partial \rho E}{\partial t} + \nabla\cdot\left[\left(h + kM^2\right)\rho\mathbf{u}\right] &= 0. \end{aligned} \tag{8}$$

Our goal is to derive the limit of the continuous model both in the case of single length scale and two-scale length. Before achieving this goal, we present the EOS that will be employed for the numerical simulations in Section 5.

2.1 The equation of state

System (8) has to be completed with an equation of state (EOS). In this work, we focus on the ideal gas law, the stiffened gas EOS (SG-EOS) [42] and the general cubic EOS [57], even though we point out that the analyses which will be carried out in Sections 2.2, 2.3, and 3 are valid for a general EOS. The equation that links together pressure, density, and internal energy for an ideal gas is given by [57]

$$p = (\gamma - 1)\,\rho e = (\gamma - 1)\left(\rho E - \frac{1}{2}M^2\rho\mathbf{u}\cdot\mathbf{u}\right). \tag{9}$$

Notice that (9) is valid only for a constant value of the specific heats ratio γ [57]. The analogous relation for the SG-EOS reads as follows:

$$p = (\gamma - 1)\,(\rho e - \rho q_\infty) - \gamma\pi_\infty = (\gamma - 1)\left(\rho E - \frac{1}{2}M^2\rho\mathbf{u}\cdot\mathbf{u} - \rho q_\infty\right) - \gamma\pi_\infty, \tag{10}$$

with q_∞ and π_∞ representing constant parameters which determine the characteristics of the fluid. Notice that for $q_\infty = \pi_\infty = 0$ in (10), we recover (9). The last relation that we consider is the general cubic EOS, for which the equation linking together internal energy, density, and temperature, is given by [47, 57]

$$e = e^{\#}(T) + \frac{a + T\frac{da}{dT}}{b}U\left(\rho, b, r_1, r_2\right). \tag{11}$$

Here, $e^{\#}(T)$ denotes the internal energy of an ideal gas at temperature T, r_1 and r_2 are suitable constants, whereas the parameters a, b determine fluid characteristics [57]. More specifically, a is related to intermolecular forces, while b, the so called co-volume, takes into account the volume occupied by the molecules. For $r_1 = r_2 = 0$ and $U = -b\rho$, we obtain the van der Waals EOS, whereas for $r_1 = -1 - \sqrt{2}, r_2 = -1 + \sqrt{2}$ and $U = \frac{1}{r_1 - r_2}\log\left(\frac{1-\rho b r_1}{1-\rho b r_2}\right)$ we get the Peng-Robinson EOS [47, 57]. We consider here constant coefficients a and b as well as $\frac{de^{\#}}{dT} = 0$. We refer to [47] for the specific numerical treatment of the general cubic EOS if $\frac{da}{dT} \neq 0$ or if $\frac{de^{\#}}{dT}$ is not constant. Finally, the equation linking pressure, density and temperature for the general cubic EOS can be expressed as follows:

$$p = \frac{\rho RT}{1 - \rho b} - \frac{a\rho^2}{(1 - \rho b r_1)\,(1 - \rho b r_2)}, \tag{12}$$

with R denoting the specific gas constant. Notice that for $a = b = 0$, we get the equation for an ideal gas, namely

$$p = \rho RT. \tag{13}$$

Hence, the equation that links internal energy, pressure, and density that we consider is the following

$$e = \frac{1 - \rho b}{\gamma - 1}\left(\frac{p}{\rho} + \frac{a\rho}{(1 - \rho b r_1)\,(1 - \rho b r_2)}\right) + \frac{a}{b}U, \tag{14}$$

with γ denoting the specific heats ratio associated to $e^{\#}$. We also recall here the expression of the speed of sound, which will be employed to compute the acoustic Courant number (see Section 5). The speed of sound is defined for a generic equation of state as [47, 57]:

$$c^2 = \left.\frac{\partial p}{\partial \rho}\right|_s = \frac{\frac{p}{\rho^2} - \frac{\partial e}{\partial \rho}}{\frac{\partial e}{\partial p}}, \tag{15}$$

with s denoting the specific entropy. Hence, for the ideal gas law (9), we get

$$c = \sqrt{\gamma \frac{p}{\rho}}. \tag{16}$$

For what concerns the SG-EOS, one obtains

$$c = \sqrt{\gamma \frac{p + \pi_\infty}{\rho}}. \tag{17}$$

Finally, the speed of sound for the general cubic EOS reads as follows:

$$\begin{aligned} c^2 &= \gamma \frac{p}{\rho} \frac{1}{1-\rho b} - \frac{a\rho}{1-\rho b}\left(\frac{\frac{\partial U}{\partial \rho}}{b}(\gamma - 1) + \frac{1 - 2\rho b}{(1-\rho b r_1)(1-\rho b r_2)}\right) \\ &- ab\rho^2 \frac{r_1(1-\rho b r_2) + r_2(1-\rho b r_1)}{(1-\rho b r_1)^2 (1-\rho b r_2)^2}, \end{aligned} \tag{18}$$

with

$$\frac{\partial U}{\partial \rho} = -\frac{b}{(1-\rho b r_1)(1-\rho b r_2)}. \tag{19}$$

Notice once more that, (18) is valid only if $\frac{da}{dT} = 0$ and $\frac{de^{\#}}{dT} = 0$.

2.2 Asymptotic expansion for single length scale

In this Section, we analyze the limit of (8) assuming that the solution depends on a single length scale. Consider the following expansion for density, momentum, pressure, and internal energy, respectively:

$$\rho(\mathbf{x},t) = \bar{\rho}(\mathbf{x},t) + M\rho^{'}(\mathbf{x},t) + M^2\rho^{''}(\mathbf{x},t) + o(M^2) \tag{20}$$

$$\begin{aligned} \rho(\mathbf{x},t)\mathbf{u}(\mathbf{x},t) &= \bar{\rho}(\mathbf{x},t)\bar{\mathbf{u}}(\mathbf{x},t) + M\rho^{'}(\mathbf{x},t)\mathbf{u}^{'}(\mathbf{x},t) \\ &+ M^2\rho^{''}(\mathbf{x},t)\mathbf{u}^{''}(\mathbf{x},t) + o(M^2) \end{aligned} \tag{21}$$

$$p(\mathbf{x},t) = \bar{p}(\mathbf{x},t) + Mp^{'}(\mathbf{x},t) + M^2p^{''}(\mathbf{x},t) + o(M^2) \tag{22}$$

$$\begin{aligned} \rho(\mathbf{x},t)e(\mathbf{x},t) &= \bar{\rho}(\mathbf{x},t)\bar{e}(\mathbf{x},t) + M\rho^{'}(\mathbf{x},t)e^{'}(\mathbf{x},t) \\ &+ M^2\rho^{''}(\mathbf{x},t)e^{''}(\mathbf{x},t) + o(M^2) \end{aligned} \tag{23}$$

From now on, for the sake of simplicity in the notation, we omit the explicit dependence on space and time for all the variables. Substituting (20) and (21) into the continuity equation in (8), the leading order term relation is

$$\frac{\partial \bar{\rho}}{\partial t} + \nabla\cdot(\bar{\rho}\bar{\mathbf{u}}) = 0. \tag{24}$$

For what concerns the momentum balance, the leading order term relation reduces to

$$\nabla \bar{p} = \mathbf{0}, \tag{25}$$

meaning that $\bar{p}$ does not depends on space. Analogously, for the first order term, we obtain

$$\nabla p^{'} = \mathbf{0}. \tag{26}$$

Moreover, the second order term reads as follows:

$$\frac{\partial \bar{\rho}\bar{\mathbf{u}}}{\partial t} + \nabla\cdot\left(\bar{\rho}\bar{\mathbf{u}} \otimes \bar{\mathbf{u}}\right) + \nabla p^{''} = \mathbf{0}, \tag{27}$$

where $p^{''}$ represents a dynamical pressure [16, 56], namely the standard pressure variable for incompressible flows [38]. Finally, the leading order term for the energy equation is

$$\frac{\partial \bar{\rho}\bar{e}}{\partial t} + \nabla\cdot\left(\bar{\rho}\bar{h}\bar{\mathbf{u}}\right) = 0. \tag{28}$$

Since $\bar{\rho}\bar{e} = \bar{\rho}\bar{h} - \bar{p}$, we obtain

$$\frac{\partial \bar{\rho}\bar{h}}{\partial t} - \frac{\partial \bar{p}}{\partial t} + \nabla\cdot\left(\bar{\rho}\bar{h}\bar{\mathbf{u}}\right) = 0, \tag{29}$$

or, equivalently,

$$\frac{\partial \bar{\rho}\bar{h}}{\partial t} - \frac{\partial \bar{p}}{\partial t} + \bar{\mathbf{u}}\cdot\nabla\left(\bar{\rho}\bar{h}\right) + \bar{\rho}\bar{h}\left(\nabla\cdot\mathbf{u}\right) = 0. \tag{30}$$

Since for a general EOS, $\bar{h} = \bar{h}\left(\bar{\rho}, \bar{p}\right)$, we get

$$\frac{\partial \bar{\rho}\bar{h}}{\partial \bar{\rho}}\left(\frac{\partial \bar{\rho}}{\partial t} + \bar{\mathbf{u}}\cdot\nabla\bar{\rho}\right) + \frac{\partial \bar{\rho}\bar{h}}{\partial \bar{p}}\left(\frac{\partial \bar{p}}{\partial t} + \bar{\mathbf{u}}\cdot\nabla\bar{p}\right) - \frac{\partial \bar{p}}{\partial t} + \bar{\rho}\bar{h}\left(\nabla\cdot\bar{\mathbf{u}}\right) = 0. \tag{31}$$

Thanks to (24) and (25), we obtain

$$\left(\bar{\rho}\bar{h} - \frac{\partial \bar{\rho}\bar{h}}{\partial \bar{\rho}}\bar{\rho}\right)\left(\nabla\cdot\bar{\mathbf{u}}\right) + \left(\frac{\partial \bar{\rho}\bar{h}}{\partial \bar{p}} - 1\right)\frac{\partial \bar{p}}{\partial t} = 0, \tag{32}$$

or, since $\bar{\rho}\bar{h} - \frac{\partial \bar{\rho}\bar{h}}{\partial \bar{\rho}}\bar{\rho} = -\bar{\rho}^2\frac{\partial \bar{h}}{\partial \bar{\rho}}$ and $\frac{\partial \bar{\rho}\bar{h}}{\partial \bar{p}} - 1 = \frac{\partial \bar{\rho}\bar{e}}{\partial \bar{p}}$, equivalently

$$-\bar{\rho}^2\frac{\partial \bar{h}}{\partial \bar{\rho}}\left(\nabla\cdot\bar{\mathbf{u}}\right) + \frac{\partial \bar{\rho}\bar{e}}{\partial \bar{p}}\frac{\partial \bar{p}}{\partial t} = 0. \tag{33}$$

Assuming $\frac{\partial \bar{p}}{\partial t} = 0$ and $\frac{\partial \bar{h}}{\partial \bar{\rho}} \neq 0$, as in [16], we recover the incompressibility constraint

$$\nabla\cdot\bar{\mathbf{u}} = 0. \tag{34}$$

Summing up, the asymptotic limit of (8) is

$$\begin{aligned}
\frac{\partial \bar{\rho}}{\partial t} + \nabla\cdot\left(\bar{\rho}\bar{\mathbf{u}}\right) &= 0 \\
\nabla \bar{p} &= \mathbf{0} \\
\nabla p^{'} &= \mathbf{0} \\
\frac{\partial \bar{\rho}\bar{\mathbf{u}}}{\partial t} + \nabla\cdot\left(\bar{\rho}\bar{\mathbf{u}} \otimes \bar{\mathbf{u}}\right) + \nabla p^{''} &= \mathbf{0} \\
\frac{\partial \bar{\rho}\bar{e}}{\partial t} + \nabla\cdot\left(\bar{\rho}\bar{h}\bar{\mathbf{u}}\right) &= 0,
\end{aligned} \tag{35}$$

or, equivalently,

$$\begin{aligned} \frac{\partial \bar{\rho}}{\partial t} + \nabla\cdot(\bar{\rho}\bar{\mathbf{u}}) &= 0 \\ \nabla \bar{p} &= \mathbf{0} \\ \nabla p^{'} &= \mathbf{0} \\ \frac{\partial \bar{\rho}\bar{\mathbf{u}}}{\partial t} + \nabla\cdot(\bar{\rho}\bar{\mathbf{u}}\otimes\bar{\mathbf{u}}) + \nabla p^{''} &= \mathbf{0} \\ -\bar{\rho}^2\frac{\partial \bar{h}}{\partial \bar{\rho}}(\nabla\cdot\bar{\mathbf{u}}) + \frac{\partial \bar{\rho}\bar{e}}{\partial \bar{p}}\frac{\partial \bar{p}}{\partial t} &= 0. \end{aligned} \tag{36}$$

Systems (35)-(36) represent the non-trivial extension to non-ideal gases of the system of equations derived in [38]. Analogous relations have been derived in [16] for the case $\frac{\partial \bar{p}}{\partial t} = 0$. However, as evident from the last relation in (36), a time dependent pressure with large amplitude variations leads to a non-incompressible flow, i.e. $\nabla\cdot\mathbf{u} \neq 0$. Hence, if $\frac{\partial \bar{h}}{\partial \bar{\rho}} \neq 0$, as it holds for most EOS, and $\frac{\partial \bar{p}}{\partial t} = 0$, all the equations of state lead to the same limit, namely the incompressible Euler equations. On the other hand, if $\frac{\partial \bar{p}}{\partial t} \neq 0$, then $\nabla\cdot\bar{\mathbf{u}}$ depends on the specific EOS. We rewrite the last relation in (36) as follows:

$$\nabla\cdot\bar{\mathbf{u}} = \frac{\frac{\partial \bar{\rho}\bar{e}}{\partial \bar{p}}}{\bar{\rho}^2\frac{\partial \bar{h}}{\partial \bar{\rho}}}\frac{\partial \bar{p}}{\partial t}, \tag{37}$$

or, equivalently,

$$\nabla\cdot\bar{\mathbf{u}} = \frac{\frac{\partial \bar{\rho}\bar{e}}{\partial \bar{p}}}{\bar{\rho}^2\frac{\partial \bar{h}}{\partial \bar{\rho}}}\frac{d\bar{p}}{dt}, \tag{38}$$

since $\bar{p}$ does not depend on space. For the ideal gas law (9), we obtain

$$\frac{\partial \bar{\rho}\bar{e}}{\partial \bar{p}} = \frac{1}{\gamma-1} \qquad \bar{\rho}^2\frac{\partial \bar{h}}{\partial \bar{\rho}} = -\frac{\gamma}{\gamma-1}\bar{p}, \tag{39}$$

so that (38) reduces to

$$\nabla\cdot\bar{\mathbf{u}} = -\frac{1}{\gamma}\frac{d\log\bar{p}}{dt}. \tag{40}$$

Hence, the compressibility of a fluid described by the ideal gas law (9) is uniform in space and changes only in time. This is no longer valid for a general EOS and, in particular, for the general cubic EOS, as we will also show in Section 5.

2.3 Asymptotic expansion for two length scales

In this Section, following [38], we assume that the solution depends also on an acoustic length scale $\boldsymbol{\xi} = M\mathbf{x}$. Hence, in a two-scale asymptotic analysis, we consider the following expansion for any dependent variable:

$$f(\mathbf{x},\boldsymbol{\xi},t) = \bar{f}(\mathbf{x},\boldsymbol{\xi},t) + Mf^{'}(\mathbf{x},\boldsymbol{\xi},t) + M^2 f^{''}(\mathbf{x},\boldsymbol{\xi},t) + o(M^2), \tag{41}$$

so that a second scale spatial derivative operator naturally appears in the asymptotic expansion. More specifically, we get

$$\nabla f = \nabla_{\mathbf{x}} f + M\,\nabla_{\boldsymbol{\xi}} f. \tag{42}$$

One can easily notice from (42) that the leading order relations are not modified introducing $\boldsymbol{\xi}$, provided that we reinterpret $\nabla\,\square$ and $\nabla\cdot\,\square$ as $\nabla_{\mathbf{x}}\,\square$ and $\nabla_{\mathbf{x}}\cdot\,\square$, respectively. Equations (26) and (27) change because of $\boldsymbol{\xi}$. Indeed, since

$$\nabla\, p = \nabla_{\mathbf{x}}\,\bar{p} + M\left(\nabla_{\mathbf{x}}\, p^{'} + \nabla_{\boldsymbol{\xi}}\,\bar{p}\right) + M^2\left(\nabla_{\mathbf{x}}\, p^{''} + \nabla_{\boldsymbol{\xi}}\, p^{'}\right) + o(M^2), \tag{43}$$

we obtain

$$\begin{aligned} \nabla_{\mathbf{x}}\, p^{'} + \nabla_{\boldsymbol{\xi}}\,\bar{p} &= \mathbf{0} && (44)\\ \frac{\partial\bar{\rho}\bar{\mathbf{u}}}{\partial t} + \nabla\cdot\left(\bar{\rho}\bar{\mathbf{u}}\otimes\bar{\mathbf{u}}\right) + \nabla_{\mathbf{x}}\, p^{''} + \nabla_{\boldsymbol{\xi}}\, p^{'} &= \mathbf{0}. && (45)\end{aligned}$$

Finally, we consider the first order term of the energy equation, which reads as follows:

$$\frac{\partial\rho^{'}e^{'}}{\partial t} + \nabla_{\mathbf{x}}\cdot\left(\rho^{'}\mathbf{u}^{'}h^{'}\right) + \nabla_{\boldsymbol{\xi}}\cdot\left(\bar{\rho}\bar{\mathbf{u}}\bar{h}\right) = 0, \tag{46}$$

or, equivalently

$$-\left(\rho^{'}\right)^2\frac{\partial h^{'}}{\partial\rho^{'}}\left(\nabla_{\mathbf{x}}\cdot\,\mathbf{u}^{'}\right) + \nabla_{\boldsymbol{\xi}}\cdot\left(\bar{\rho}\bar{\mathbf{u}}\bar{h}\right) + \frac{\partial\rho^{'}e^{'}}{\partial p^{'}}\frac{\partial p^{'}}{\partial t} = 0. \tag{47}$$

Summing up, the asymptotic limit of (8) for a two-scale analysis is

$$\begin{aligned} \frac{\partial\bar{\rho}}{\partial t} + \nabla_{\mathbf{x}}\cdot\left(\bar{\rho}\bar{\mathbf{u}}\right) &= 0\\ \nabla_{\mathbf{x}}\,\bar{p} &= \mathbf{0}\\ \nabla_{\mathbf{x}}\, p^{'} + \nabla_{\boldsymbol{\xi}}\,\bar{p} &= \mathbf{0}\\ \frac{\partial\bar{\rho}\bar{\mathbf{u}}}{\partial t} + \nabla_{\mathbf{x}}\cdot\left(\bar{\rho}\bar{\mathbf{u}}\otimes\bar{\mathbf{u}}\right) + \nabla_{\mathbf{x}}\, p^{''} + \nabla_{\boldsymbol{\xi}}\, p^{'} &= \mathbf{0}\\ \frac{\partial\bar{\rho}\bar{e}}{\partial t} + \nabla_{\mathbf{x}}\cdot\left(\bar{\rho}\bar{h}\bar{\mathbf{u}}\right) &= 0\\ \frac{\partial\rho^{'}e^{'}}{\partial t} + \nabla_{\mathbf{x}}\cdot\left(\rho^{'}\mathbf{u}^{'}h^{'}\right) + \nabla_{\boldsymbol{\xi}}\cdot\left(\bar{\rho}\bar{h}\bar{\mathbf{u}}\right) &= 0, \end{aligned} \tag{48}$$

or, equivalently,

$$\begin{aligned} \frac{\partial\bar{\rho}}{\partial t} + \nabla_{\mathbf{x}}\cdot\left(\bar{\rho}\bar{\mathbf{u}}\right) &= 0\\ \nabla_{\mathbf{x}}\,\bar{p} &= \mathbf{0}\\ \nabla_{\mathbf{x}}\, p^{'} + \nabla_{\boldsymbol{\xi}}\,\bar{p} &= \mathbf{0}\\ \frac{\partial\bar{\rho}\bar{\mathbf{u}}}{\partial t} + \nabla_{\mathbf{x}}\cdot\left(\bar{\rho}\bar{\mathbf{u}}\otimes\bar{\mathbf{u}}\right) + \nabla_{\mathbf{x}}\, p^{''} + \nabla_{\boldsymbol{\xi}}\, p^{'} &= \mathbf{0}\\ -\bar{\rho}^2\frac{\partial\bar{h}}{\partial\bar{\rho}}\left(\nabla_{\mathbf{x}}\cdot\,\bar{\mathbf{u}}\right) + \frac{\partial\bar{\rho}\bar{e}}{\partial\bar{p}}\frac{\partial\bar{p}}{\partial t} &= 0\\ -\left(\rho^{'}\right)^2\frac{\partial h^{'}}{\partial\rho^{'}}\left(\nabla_{\mathbf{x}}\cdot\,\mathbf{u}^{'}\right) + \nabla_{\boldsymbol{\xi}}\cdot\left(\bar{\rho}\bar{\mathbf{u}}\bar{h}\right) + \frac{\partial\rho^{'}e^{'}}{\partial p^{'}}\frac{\partial p^{'}}{\partial t} &= 0. \end{aligned} \tag{49}$$

Analogous considerations to those discussed in Section 2.2 are valid for the leading order term relations. Following the discussion in [38], we consider two different regimes.

In the first regime, one assumes that the characteristic length of the system is comparable to the reference length $\mathcal{L}$. Hence, we recover the single length scale model already discussed in Section 2.2. We consider now a second regime, for which the characteristic length of the system is large compared to the reference length $\mathcal{L}$, so that the acoustic scale carries relevant information. We assume therefore that the flow has variations only on the large acoustic scale. The $\mathbf{x}-$averaged equations obtained starting from (48)-(49) read as follows:

$$\begin{aligned} \frac{\partial \bar{\rho}}{\partial t} &= 0 \\ \frac{\partial \bar{\rho}\bar{\mathbf{u}}}{\partial t} + \nabla_{\boldsymbol{\xi}} p^{'} &= \mathbf{0} \\ \nabla_{\boldsymbol{\xi}} \bar{p} &= 0 \\ \frac{\partial \bar{p}}{\partial t} &= 0 \\ \frac{\partial \rho^{'} e^{'}}{\partial t} + \nabla_{\boldsymbol{\xi}} \cdot \left(\bar{\rho}\bar{\mathbf{u}}\bar{h}\right) &= 0. \end{aligned} \tag{50}$$

The relation $\frac{\partial \bar{p}}{\partial t} = 0$ is a direct consequence of the fact that, in the regime of interest, $\nabla_{\mathbf{x}} \cdot \bar{\mathbf{u}} = 0$. Moreover, we notice that $\bar{p}$ reduces to a constant. In the particular case of the ideal gas law (9), (50) reduces to

$$\begin{aligned} \frac{\partial \bar{\rho}}{\partial t} &= 0 \\ \frac{\partial \bar{\mathbf{u}}}{\partial t} + \frac{1}{\bar{\rho}\left(\boldsymbol{\xi}\right)} \nabla_{\boldsymbol{\xi}} p^{'} &= \mathbf{0} \\ \nabla_{\boldsymbol{\xi}} \bar{p} &= 0 \\ \frac{\partial \bar{p}}{\partial t} &= 0 \\ \frac{\partial p^{'}}{\partial t} + \gamma \bar{p} \nabla_{\boldsymbol{\xi}} \cdot \bar{\mathbf{u}} &= 0. \end{aligned} \tag{51}$$

Taking the time derivative of the last equation, we obtain

$$\frac{\partial^2 p^{'}}{\partial t^2} + \nabla_{\boldsymbol{\xi}} \cdot \left(\bar{c}^2\left(\boldsymbol{\xi}\right) \nabla_{\boldsymbol{\xi}} p^{'}\right), \tag{52}$$

with $\bar{c}^2 = \gamma \frac{\bar{p}}{\bar{\rho}}$. Equation 52 is the wave equation for $p^{'}$ already derived in [38]. Relation (52) is instead no longer valid for a general EOS.

3 Asymptotic analysis for a class of IMEX-ARK schemes

We analyze now the AP property of a general class of IMEX-ARK schemes, built on the experience of the numerical method presented in [46, 47, 48] for (8). Following [12, 19], we couple implicitly the energy equation to the momentum one, while the continuity equation is discretized in a fully explicit fashion. Hence, we obtain a non-linear

Helmholtz equation for the pressure, which is solved through a fixed point procedure [19, 47]. We consider an Implicit-Explicit Additive Runge Kutta (IMEX-ARK) scheme for the time discretization [36]. IMEX-ARK methods are represented compactly by the following two Butcher tableaux [11]:

$$\begin{array}{c|c} \mathbf{c} & \mathbf{A} \\ \hline & \mathbf{b}^T \end{array} \qquad \begin{array}{c|c} \tilde{\mathbf{c}} & \tilde{\mathbf{A}} \\ \hline & \tilde{\mathbf{b}}^T \end{array}$$

with $\mathbf{A} = \{A_{ij}\}, \mathbf{b} = \{b_i\}, \mathbf{c} = \{c_i\}, \tilde{\mathbf{A}} = \left\{\tilde{A}_{ij}\right\}, \tilde{\mathbf{b}} = \left\{\tilde{b}_i\right\}$, and $\tilde{\mathbf{c}} = \{\tilde{c}_i\}$. Coefficients $A_{ij}, \tilde{A}_{ij}, c_i, \tilde{c}_i, b_i$, and $\tilde{b}_i$ are determined so that the method is consistent of a given order. In particular, the following relation has to be satisfied [36]:

$$\sum_i b_i = \sum_i \tilde{b}_i = 1. \tag{53}$$

Following the Butcher tableaux introduced above, for a time dependent problem

$$\frac{d\mathbf{y}}{dt} = \mathbf{f}_E(\mathbf{y}, t) + \mathbf{f}_I(\mathbf{y}, t), \tag{54}$$

the generic s-stage of an IMEX-ARK method can be defined as

$$\begin{aligned} \mathbf{v}^{(n,l)} &= \mathbf{v}^n + \Delta t \sum_{m=1}^{l-1} a_{lm} \mathbf{f}_E\left(\mathbf{v}^{(n,m)}, t^n + c_m \Delta t\right) \\ &+ \Delta t \sum_{m=1}^{l} \tilde{a}_{lm} \mathbf{f}_I\left(\mathbf{v}^{(n,m)}, t^n + \tilde{c}_m \Delta t\right), \end{aligned} \tag{55}$$

where $l = 1, \ldots, s$, Δt is the time discretization step, $\mathbf{v}^n \approx \mathbf{y}(t^n)$, $\mathbf{f}_E$ is the spatial term treated explicitly, and $\mathbf{f}_I$ is the spatial term treated implicitly. After computation of the intermediate stages, the updated solution is computed as follows:

$$\mathbf{v}^{n+1} = \mathbf{v}^n + \Delta t \sum_{l=1}^{s} b_l \mathbf{f}_E\left(\mathbf{v}^{(n,l)}, t^n + c_l \Delta t\right) + \Delta t \sum_{l=1}^{s} \tilde{b}_l \mathbf{f}_I\left(\mathbf{v}^{(n,l)}, t^n + \tilde{c}_l \Delta t\right). \tag{56}$$

The formulation (55)-(56) is valid for an IMEX scheme of arbitrary order. We recall that implicit methods of order higher than one for hyperbolic problems cannot be unconditionally total variation diminishing (TVD) [25] and this is valid also when IMEX methods are employed [7, 18]. In this work, as done e.g. in [7], we do not focus on this limit imposed by high order schemes and we consider therefore numerical methods which, in principle, may not guarantee L^∞-stability. Notice also that, the existence of the Hilbert expansion (59) can be justified only for smooth functions [41]. The development of a numerical treatment to avoid this issue goes beyond the scope of the present work and will be carried out as future development. For our analysis, we assume $\mathbf{c} = \tilde{\mathbf{c}}$ and that

$$\sum_j A_{ij} = c_i \qquad \sum_j \tilde{A}_{ij} = \tilde{c}_i \tag{57}$$

Relation (57) is an usual assumption for Runge Kutta schemes [6, 36]. The assumption $\mathbf{c} = \tilde{\mathbf{c}}$ is less common, but it has been employed e.g. in [3, 7]. Finally, we also assume

that the implicit scheme is a Diagonally Implicit Runge Kutta (DIRK) method, namely $\tilde{A}_{ij} = 0$ for $i > j$. Hence, a generic stage of the Euler equations reads as follows:

$$\begin{aligned}
\rho^{(n,l)} &= \rho^n - \sum_{m=1}^{l-1} a_{lm}\Delta t\, \nabla\cdot\left(\rho^{(n,m)}\mathbf{u}^{(n,m)}\right) \\
\rho^{(n,l)}\mathbf{u}^{(n,l)} + \frac{1}{M^2}\tilde{a}_{ll}\Delta t\, \nabla p^{(n,l)} &= \rho^n\mathbf{u}^n \\
&- \sum_{m=1}^{l-1} a_{lm}\Delta t\, \nabla\cdot\left(\rho^{(n,m)}\mathbf{u}^{(n,m)}\otimes\mathbf{u}^{(n,m)}\right) \\
&- \frac{1}{M^2}\sum_{m=1}^{l-1} \tilde{a}_{lm}\Delta t\, \nabla p^{(n,m)} \qquad (58) \\
\rho^{(n,l)}E^{(n,l)} + \tilde{a}_{ll}\Delta t\, \nabla\cdot\left(h^{(n,l)}\rho^{(n,l)}\mathbf{u}^{(n,l)}\right) &= \rho^n E^n \\
&- \sum_{m=1}^{l-1} \tilde{a}_{lm}\Delta t\, \nabla\cdot\left(h^{(n,m)}\rho^{(n,m)}\mathbf{u}^{(n,m)}\right) \\
&- \sum_{m=1}^{l-1} a_{lm}\Delta t M^2\, \nabla\cdot\left(k^{(n,m)}\rho^{(n,m)}\mathbf{u}^{(n,m)}\right).
\end{aligned}$$

We analyze now the time semi-discretization for $M \to 0$, so as to verify that it provides a consistent semi-discretization for the two limit models identified in Section 2.2 and Section 2.3, respectively.

3.1 Asymptotic analysis in the single length scale case

In this Section, we consider the limit model (35)-(36). Following e.g. [41], we make the assumption that, at each stage, the discrete quantities admit a formal expansion analogous to the continuous case.

Assumption 3.1. *The physical variables $\rho, \rho\mathbf{u}, p$, and ρe admit at each stage a formal Hilbert expansion of the form (written e.g. for ρ^n)*

$$\rho^n(\mathbf{x}) = \bar{\rho}^n(\mathbf{x}) + M\rho^{'n}(\mathbf{x}) + M^2\rho^{''n}(\mathbf{x}) + o(M^2). \qquad (59)$$

We also make the following assumption:

Assumption 3.2. *The initial datum p^0 is well-prepared, namely $\nabla\bar{p}^0 = \nabla p^{'0} = \mathbf{0}$.*

Then, the following result holds:

Lemma 3.3. *Under Assumption 3.1 and Assumption 3.2,* (58) *provides a consistent discretization of* (35)-(36)*.*

Proof. We plug asymptotic expansions of the form (59) into (58). The discrete limit

system reads therefore as follows:

$$
\begin{aligned}
\bar{\rho}^{(n,l)} &= \bar{\rho}^{n} - \sum_{m=1}^{l-1} a_{lm}\Delta t\,\nabla\cdot\left(\bar{\rho}^{(n,m)}\bar{\mathbf{u}}^{(n,m)}\right)\\
\tilde{a}_{ll}\,\nabla\,\bar{p}^{(n,l)} &= -\sum_{m=1}^{l-1}\tilde{a}_{lm}\,\nabla\,\bar{p}^{(n,m)}\\
\tilde{a}_{ll}\,\nabla\,p^{'(n,l)} &= -\sum_{m=1}^{l-1}\tilde{a}_{lm}\,\nabla\,p^{'(n,m)}\\
\bar{\rho}^{(n,l)}\bar{\mathbf{u}}^{(n,l)} + \tilde{a}_{ll}\Delta t\,\nabla\,p^{''(n,l)} &= \bar{\rho}^{n}\bar{\mathbf{u}}^{n}\\
&- \sum_{m=1}^{l-1} a_{lm}\Delta t\,\nabla\cdot\left(\bar{\rho}^{(n,m)}\bar{\mathbf{u}}^{(n,m)}\otimes\bar{\mathbf{u}}^{(n,m)}\right)\\
&- \sum_{m=1}^{l-1}\tilde{a}_{lm}\Delta t\,\nabla\,p^{''(n,m)}\\
\bar{\rho}^{(n,l)}\bar{e}^{(n,l)} + \tilde{a}_{ll}\Delta t\,\nabla\cdot\left(\bar{h}^{(n,l)}\bar{\rho}^{(n,l)}\bar{\mathbf{u}}^{(n,l)}\right) &= \bar{\rho}^{n}\bar{e}^{n}\\
&- \sum_{m=1}^{l-1}\tilde{a}_{lm}\Delta t\,\nabla\cdot\left(\bar{h}^{(n,m)}\bar{\rho}^{(n,m)}\bar{\mathbf{u}}^{(n,m)}\right),
\end{aligned}
\tag{60}
$$

which, thanks to Assumption (3.2), is clearly a consistent discretization of (35). Nevertheless, we want to show that the last relation yields a consistent discretization for (33), so as to prove that (60) is a consistent discretization of (36). After a few manipulations, taking into account that $\nabla\,\bar{p}^{(n,l)} = \mathbf{0}$, we get

$$
\begin{aligned}
&\bar{\rho}^{(n,l)}\bar{h}^{(n,l)} - \bar{p}^{(n,l)}\\
+\;&\tilde{a}_{ll}\Delta t\left[\bar{\rho}^{(n,l)}\bar{h}^{(n,l)}\left(\nabla\cdot\,\bar{\mathbf{u}}^{(n,l)}\right) + \bar{\mathbf{u}}^{(n,l)}\cdot\nabla\,\bar{\rho}^{(n,l)}\frac{\partial\bar{\rho}^{(n,l)}\bar{h}^{(n,l)}}{\partial\bar{\rho}^{(n,l)}}\right] =\\
&\bar{\rho}^{n}\bar{h}^{n} - \bar{p}^{n}\\
-\;&\sum_{m=1}^{l-1}\tilde{a}_{lm}\Delta t\left[\bar{\rho}^{(n,m)}\bar{h}^{(n,m)}\left(\nabla\cdot\,\bar{\mathbf{u}}^{(n,m)}\right) + \bar{\mathbf{u}}^{(\mathbf{n},\mathbf{m})}\cdot\nabla\,\bar{\rho}^{(n,m)}\frac{\partial\bar{\rho}^{(n,m)}\bar{h}^{(n,m)}}{\partial\bar{\rho}^{(n,m)}}\right].
\end{aligned}
\tag{61}
$$

The error obtained applying (61) to the exact solution reads therefore as follows:

$$
\begin{aligned}
\hat{\tau}^{(n,l)} &= \bar{\rho}\left(\mathbf{x},t^{n}+c_{l}\Delta t\right)\bar{h}\left(\mathbf{x},t^{n}+c_{l}\Delta t\right) - \bar{\rho}\left(\mathbf{x},t^{n}\right)\bar{h}\left(\mathbf{x},t^{n}\right)\\
&- \left[\bar{p}\left(\mathbf{x},t^{n}+c_{l}\Delta t\right) - \bar{p}\left(\mathbf{x},t^{n}\right)\right]\\
&+ \tilde{a}_{ll}\Delta t\left[\bar{\rho}\left(\mathbf{x},t^{n}+c_{l}\Delta t\right)\bar{h}\left(\mathbf{x},t^{n}+c_{l}\Delta t\right)\left(\nabla\cdot\,\bar{\mathbf{u}}\left(\mathbf{x},t^{n}+c_{l}\Delta t\right)\right)\right]\\
&+ \tilde{a}_{ll}\Delta t\left[\bar{\mathbf{u}}\left(\mathbf{x},t^{n}+c_{l}\Delta t\right)\cdot\nabla\,\bar{\rho}\left(\mathbf{x},t^{n}+c_{l}\Delta t\right)\frac{\partial\bar{\rho}\bar{h}}{\partial\bar{\rho}}\left(\mathbf{x},t^{n}+c_{l}\Delta t\right)\right]\\
&+ \sum_{m=1}^{l-1}\tilde{a}_{lm}\Delta t\left[\bar{\rho}\left(\mathbf{x},t^{n}+c_{m}\Delta t\right)\bar{h}\left(\mathbf{x},t^{n}+c_{m}\Delta t\right)\left(\nabla\cdot\,\bar{\mathbf{u}}\left(\mathbf{x},t^{n}+c_{m}\Delta t\right)\right)\right]\\
&+ \sum_{m=1}^{l-1}\tilde{a}_{lm}\Delta t\left[\bar{\mathbf{u}}\left(\mathbf{x},t^{n}+c_{m}\Delta t\right)\cdot\nabla\,\bar{\rho}\left(\mathbf{x},t^{n}+c_{m}\Delta t\right)\frac{\partial\bar{\rho}\bar{h}}{\partial\bar{\rho}}\left(\mathbf{x},t^{n}+c_{m}\Delta t\right)\right].
\end{aligned}
\tag{62}
$$

Since $\bar{\rho}\bar{h} = \bar{\rho}\bar{h}\left(\bar{\rho}, \bar{p}\right)$, using a Taylor expansion, we get

$$\begin{aligned}
\bar{\rho}\left(\mathbf{x}, t^n + c_l\Delta t\right)\bar{h}\left(\mathbf{x}, t^n + c_l\Delta t\right) &= \bar{\rho}\left(\mathbf{x}, t^n\right)\bar{h}\left(\mathbf{x}, t^n\right) \\
&+ \frac{\partial\bar{\rho}\bar{h}}{\partial\bar{\rho}}\left(\mathbf{x}, t^n\right)\left[\bar{\rho}\left(\mathbf{x}, t^n + c_l\Delta t\right) - \bar{\rho}\left(\mathbf{x}, t^n\right)\right] \\
&+ \frac{\partial\bar{\rho}\bar{h}}{\partial\bar{p}}\left(\mathbf{x}, t^n\right)\left[\bar{p}\left(\mathbf{x}, t^n + c_l\Delta t\right) - \bar{p}\left(\mathbf{x}, t^n\right)\right] \\
&+ o\left(\bar{\rho}\left(\mathbf{x}, t^n + c_l\Delta t\right) - \bar{\rho}\left(\mathbf{x}, t^n\right)\right) \\
&+ o\left(\bar{p}\left(\mathbf{x}, t^n + c_l\Delta t\right) - \bar{p}\left(\mathbf{x}, t^n\right)\right).
\end{aligned} \tag{63}$$

Employing now the discretization of the continuity equation in (60) and the assumption (57), we obtain

$$\begin{aligned}
\bar{\rho}\left(\mathbf{x}, t^n + c_l\Delta t\right)\bar{h}\left(\mathbf{x}, t^n + c_l\Delta t\right) &= \bar{\rho}\left(\mathbf{x}, t^n\right)\bar{h}\left(\mathbf{x}, t^n\right) \\
&- c_l\Delta t\frac{\partial\bar{\rho}\bar{h}}{\partial\bar{\rho}}\left(\mathbf{x}, t^n\right)\nabla\cdot\left(\bar{\rho}^n\left(\mathbf{x}, t^n\right)\bar{\mathbf{u}}^n\left(\mathbf{x}, t^n\right)\right) \\
&+ \frac{\partial\bar{\rho}\bar{h}}{\partial\bar{p}}\left(\mathbf{x}, t^n\right)\left[\bar{p}\left(\mathbf{x}, t^n + c_l\Delta t\right) - \bar{p}\left(\mathbf{x}, t^n\right)\right] \\
&+ o\left(\bar{\rho}\left(\mathbf{x}, t^n + c_l\Delta t\right) - \bar{\rho}\left(\mathbf{x}, t^n\right)\right) \\
&+ o\left(\bar{p}\left(\mathbf{x}, t^n + c_l\Delta t\right) - \bar{p}\left(\mathbf{x}, t^n\right)\right),
\end{aligned} \tag{64}$$

or, equivalently,

$$\begin{aligned}
\bar{\rho}\left(\mathbf{x}, t^n + c_l\Delta t\right)\bar{h}\left(\mathbf{x}, t^n + c_l\Delta t\right) &= \bar{\rho}\left(\mathbf{x}, t^n\right)\bar{h}\left(\mathbf{x}, t^n\right) \\
&- c_l\Delta t\frac{\partial\bar{\rho}\bar{h}}{\partial\bar{\rho}}\left(\mathbf{x}, t^n\right)\bar{\rho}^n\left(\mathbf{x}, t^n\right)\left(\nabla\cdot\bar{\mathbf{u}}^n\left(\mathbf{x}, t^n\right)\right) \\
&- c_l\Delta t\frac{\partial\bar{\rho}\bar{h}}{\partial\bar{\rho}}\left(\mathbf{x}, t^n\right)\bar{\mathbf{u}}^n\left(\mathbf{x}, t^n\right)\cdot\nabla\,\bar{\rho}^n\left(\mathbf{x}, t^n\right) \\
&+ \frac{\partial\bar{\rho}\bar{h}}{\partial\bar{p}}\left(\mathbf{x}, t^n\right)\left[\bar{p}\left(\mathbf{x}, t^n + c_l\Delta t\right) - \bar{p}\left(\mathbf{x}, t^n\right)\right] \\
&+ o\left(\bar{\rho}\left(\mathbf{x}, t^n + c_l\Delta t\right) - \bar{\rho}\left(\mathbf{x}, t^n\right)\right) \\
&+ o\left(\bar{p}\left(\mathbf{x}, t^n + c_l\Delta t\right) - \bar{p}\left(\mathbf{x}, t^n\right)\right),
\end{aligned} \tag{65}$$

Using again a Taylor expansion, we get

$$\begin{aligned}
\bar{\rho}\left(\mathbf{x}, t^n + c_l\Delta t\right) &= \bar{\rho}\left(\mathbf{x}, t^n\right) + c_l\Delta t\frac{\partial\bar{\rho}}{\partial t}\left(\mathbf{x}, t^n\right) + o(\Delta t) \\
\bar{\mathbf{u}}\left(\mathbf{x}, t^n + c_l\Delta t\right) &= \bar{\mathbf{u}}\left(\mathbf{x}, t^n\right) + c_l\Delta t\frac{\partial\bar{\mathbf{u}}}{\partial t}\left(\mathbf{x}, t^n\right) + o(\Delta t) \\
\bar{p}\left(\mathbf{x}, t^n + c_l\Delta t\right) &= \bar{p}\left(\mathbf{x}, t^n\right) + c_l\Delta t\frac{\partial\bar{p}}{\partial t}\left(\mathbf{x}, t^n\right) + o(\Delta t).
\end{aligned} \tag{66}$$

Substituting (65) and (66) into (62), we obtain

$$\begin{aligned}\hat{\tau}^{(n,l)} &= -c_l\Delta t\frac{\partial\bar{\rho}\bar{h}}{\partial\bar{\rho}}\left(\mathbf{x},t^n\right)\bar{\rho}\left(\mathbf{x},t^n\right)\nabla\cdot\left(\bar{\mathbf{u}}^n\left(\mathbf{x},t^n\right)\right)-c_l\Delta t\frac{\partial\bar{\rho}\bar{h}}{\partial\bar{\rho}}\left(\mathbf{x},t^n\right)\bar{\mathbf{u}}^n\left(\mathbf{x},t^n\right)\cdot\nabla\bar{\rho}^n\left(\mathbf{x},t^n\right)\\ &+ \left(\frac{\partial\bar{\rho}\bar{h}}{\partial\bar{p}}\left(\mathbf{x},t^n\right)-1\right)c_l\Delta t\frac{\partial\bar{p}}{\partial t}\left(\mathbf{x},t^n\right)+\sum_{m=1}^{l}\tilde{a}_{lm}\Delta t\left[\bar{\rho}\left(\mathbf{x},t^n\right)\bar{h}\left(\mathbf{x},t^n\right)\left(\nabla\cdot\bar{\mathbf{u}}\left(\mathbf{x},t^n\right)\right)\right] \quad (67)\\ &+ \sum_{m=1}^{l}\tilde{a}_{lm}\Delta t\left[\bar{\mathbf{u}}\left(\mathbf{x},t^n\right)\cdot\nabla\bar{\rho}\left(\mathbf{x},t^n\right)\frac{\partial\bar{\rho}\bar{h}}{\partial\bar{\rho}}\left(\mathbf{x},t^n\right)\right]+o\left(\Delta t\right).\end{aligned}$$

Since $\sum_{m=1}^{l}\tilde{a}_{lm}=c_l$ (57) and $\bar{\rho}\left(\mathbf{x},t^n\right)\bar{h}\left(\mathbf{x},t^n\right)-\frac{\partial\bar{\rho}\bar{h}}{\partial\bar{\rho}}\left(\mathbf{x},t^n\right)\bar{\rho}\left(\mathbf{x},t^n\right)=-\bar{\rho}^2\left(\mathbf{x},t^n\right)\frac{\partial\bar{h}}{\partial\bar{\rho}}\left(\mathbf{x},t^n\right)$, we obtain

$$\begin{aligned}\hat{\tau}^{(n,l)} &= -c_l\Delta t\bar{\rho}^2\left(\mathbf{x},t^n\right)\frac{\partial\bar{h}}{\partial\bar{\rho}}\left(\mathbf{x},t^n\right)\nabla\cdot\left(\bar{\mathbf{u}}^n\left(\mathbf{x},t^n\right)\right)\\ &+ \left(\frac{\partial\bar{\rho}\bar{h}}{\partial\bar{p}}\left(\mathbf{x},t^n\right)-1\right)c_l\Delta t\frac{\partial\bar{p}}{\partial t}\left(\mathbf{x},t^n\right)+o\left(\Delta t\right)=o\left(\Delta t\right), \quad (68)\end{aligned}$$

thanks to (33). □

Moreover, since we are considering an implicit coupling between the momentum and the energy balance, the stability condition of the numerical method does not depend on M and on the acoustic speed of sound (see e.g. [12, 19, 53]), meaning that (58) provides an AP scheme for (35)-(36). The numerical method is not in general strongly asymptotic-preserving, namely it is not asymptotic-preserving for general initial data. More specifically, we need a well-prepared initial datum for the pressure (see Assumption 3.2). However, no restrictions are required for the initial datum of the velocity, as we will also verify numerically in Section 5.2. Hence, we do not need a divergence-free initial velocity field, unlike the weakly AP scheme developed e.g. in [44]. This is particularly important because, as already discussed in Section 3.1, $\nabla\cdot\bar{\mathbf{u}}=0$ is the asymptotic limit only if $\frac{\partial\bar{p}}{\partial t}=0$, which is not always valid. Notice also that, Assumption 3.2 can be removed considering implicit schemes for which $\tilde{\mathbf{A}}$ is diagonal, which represent a particular case of the general class of time discretization schemes discussed in this Section. This goal can be achieved considering, for instance, the implicit Euler method for a first order scheme, as done in [16], or the second order Ascher, Ruuth and Spiteri (ARS) method [3], as done in [7].

3.2 Asymptotic analysis for two length scales

In this Section, we consider the limit model (48)- (49). We replace Assumption 3.1 with the following one:

Assumption 3.4. *The physical variables $\rho, \rho\mathbf{u}, p$, and ρe admit at each stage a formal Hilbert expansion of the form (written e.g. for ρ^n)*

$$\rho^n\left(\mathbf{x},\boldsymbol{\xi}\right)=\bar{\rho}^n\left(\mathbf{x},\boldsymbol{\xi}\right)+M\rho^{'n}\left(\mathbf{x},\boldsymbol{\xi}\right)+M^2\rho^{''n}\left(\mathbf{x},\boldsymbol{\xi}\right)+o(M^2), \quad (69)$$

with $\boldsymbol{\xi}=M\mathbf{x}$.

Moreover, we replace Assumption 3.2 with the

Assumption 3.5. *The initial datum p^0 is well-prepared, namely* $\nabla_{\mathbf{x}} \bar{p}^0 = \nabla_{\mathbf{x}} \bar{p}^{'} = \nabla_{\boldsymbol{\xi}} p^{'} = \mathbf{0}$.

Then, the following result holds:

Lemma 3.6. *Under Assumption 3.4 and Assumption 3.5,* (58) *provides an AP scheme for* (48)-(49).

Proof. As pointed out for the continuous model, the leading order term relations do not change considering the length scale $\boldsymbol{\xi} = M\mathbf{x}$. We plug asymptotic expansion of the form (69) into the semi-discretized momentum equation, so as to obtain for the first order term

$$\tilde{a}_{ll} \nabla_{\mathbf{x}} p^{',(n,l)} + \tilde{a}_{ll} \nabla_{\boldsymbol{\xi}} \bar{p}^{(n,l)} = - \sum_{m=1}^{l-1} \tilde{a}_{lm} \nabla_{\mathbf{x}} p^{',(n,m)} - \sum_{m=1}^{l-1} \tilde{a}_{lm} \nabla_{\boldsymbol{\xi}} \bar{p}^{(n,m)}, \tag{70}$$

which, thanks to Assumption 3.5, is a consistent discretization of (44). For what concerns the second order term, we get

$$\begin{aligned} \bar{\rho}^{(n,2)} \mathbf{u}^{(n,2)} + \tilde{a}_{ll} \Delta t \left(\nabla_{\mathbf{x}} p^{(n,2),''} + \nabla_{\boldsymbol{\xi}} p^{(n,2),'} \right) &= \bar{\rho}^n \bar{\mathbf{u}}^n \\ &- \sum_{m=1}^{l-1} a_{lm} \Delta t \nabla_{\mathbf{x}} \cdot (\bar{\rho}^n \bar{\mathbf{u}} \otimes \bar{\mathbf{u}}) \\ &- \sum_{m=1}^{l-1} \tilde{a}_{lm} \Delta t \left(\nabla_{\mathbf{x}} p^{'',n} + \nabla_{\boldsymbol{\xi}} p^{',n} \right), \end{aligned} \tag{71}$$

which is a consistent discretization of (45). Finally, for the first order term in the energy equation, we obtain

$$\begin{aligned} &\rho^{',(n,l)} e^{',(n,l)} + \tilde{a}_{ll} \Delta t \nabla_{\mathbf{x}} \cdot \left(h^{',(n,l)} \rho^{',(n,l)} \mathbf{u}^{',(n,l)} \right) + \tilde{a}_{ll} \Delta t \nabla_{\boldsymbol{\xi}} \cdot \left(\bar{h}^{(n,l)} \bar{\rho}^{(n,l)} \bar{\mathbf{u}}^{(n,l)} \right) = \\ &\bar{\rho}^n \bar{e}^n - \sum_{m=1}^{l-1} \tilde{a}_{lm} \Delta t \nabla_{\mathbf{x}} \cdot \left(h^{',(n,m)} \rho^{',(n,m)} \mathbf{u}^{',(n,m)} \right) \\ - &\sum_{m=1}^{l-1} \tilde{a}_{lm} \Delta t \nabla_{\boldsymbol{\xi}} \cdot \left(\bar{h}^{(n,m)} \bar{\rho}^{(n,m)} \bar{\mathbf{u}}^{(n,m)} \right), \end{aligned} \tag{72}$$

which is a consistent discretization of (46). Hence, (58) provides an AP scheme for (48)-(49). □

Analogous considerations to those reported in Section 3.1 hold for the initial data.

4 Spatial discretization

In this Section, we briefly outline the spatial discretization for (58), which is based on the Discontinuous Galerkin (DG) method [23] as implemented in the *deal.II* library

[2, 4]. More specifically, the shape functions correspond to the products of Lagrange polynomials for the support points of $(r+1)$-order Gauss-Lobatto quadrature rule in each coordinate direction, where r is the polynomial degree. However, the proposed approach can also be applied to tetrahedral meshes and P-spaces. We consider a decomposition of the domain Ω into a family of quadrilaterals $\mathcal{T}_h$ and denote each element by K. We denote by $\mathcal{E}$ the set of all the element faces, so that $\mathcal{E} = \mathcal{E}^I \cup \mathcal{E}^B$, with $\mathcal{E}^I$ and $\mathcal{E}^B$ denoting the subset of interior and boundary faces, respectively. A face $\Gamma \in \mathcal{E}_I$ shares two elements, K^+ with outward unit normal $\mathbf{n}^+$ and K^- with outward unit normal $\mathbf{n}^-$. Finally, we denote by $\mathbf{n}$ the outward unit normal for a face $\Gamma \in \mathcal{E}^B$. Hence, for a scalar function φ, we define the jump as

$$[[\varphi]] = \varphi^+ \mathbf{n}^+ + \varphi^- \mathbf{n}^- \text{ if } \Gamma \in \mathcal{E}^I \qquad [[\varphi]] = \varphi \mathbf{n} \text{ if } \Gamma \in \mathcal{E}^B, \tag{73}$$

where we define the average as

$$\{\{\varphi\}\} = \frac{1}{2}\left(\varphi^+ + \varphi^-\right) \text{ if } \Gamma \in \mathcal{E}^I \qquad \{\{\varphi\}\} = \varphi \text{ if } \Gamma \in \mathcal{E}^B. \tag{74}$$

Analogous definitions apply for a vector function $\boldsymbol{\varphi}$. More specifically, we define

$$[[\boldsymbol{\varphi}]] = \boldsymbol{\varphi}^+ \cdot \mathbf{n}^+ + \boldsymbol{\varphi}^- \cdot \mathbf{n}^- \text{ if } \Gamma \in \mathcal{E}^I \qquad [[\boldsymbol{\varphi}]] = \boldsymbol{\varphi} \cdot \mathbf{n} \text{ if } \Gamma \in \mathcal{E}^B \tag{75}$$

$$\{\{\boldsymbol{\varphi}\}\} = \frac{1}{2}\left(\boldsymbol{\varphi}^+ + \boldsymbol{\varphi}^-\right) \text{ if } \Gamma \in \mathcal{E}^I \qquad \{\{\boldsymbol{\varphi}\}\} = \boldsymbol{\varphi} \text{ if } \Gamma \in \mathcal{E}^B. \tag{76}$$

For vector functions, it is also useful to define a tensor jump as follows:

$$\langle\langle\boldsymbol{\varphi}\rangle\rangle = \boldsymbol{\varphi}^+ \otimes \mathbf{n}^+ + \boldsymbol{\varphi}^- \otimes \mathbf{n}^- \text{ if } \Gamma \in \mathcal{E}^I \qquad \langle\langle\boldsymbol{\varphi}\rangle\rangle = \boldsymbol{\varphi} \otimes \mathbf{n} \text{ if } \Gamma \in \mathcal{E}^B. \tag{77}$$

Given these definitions, the weak formulation for the momentum equation at each stage (58) reads as follows [47, 48]:

$$\mathbf{A}^{(n,l)}\mathbf{U}^{(n,l)} + \mathbf{B}^{(n,l)}\mathbf{P}^{(n,l)} = \mathbf{F}^{(n,l)}, \tag{78}$$

with $\mathbf{U}^{(n,l)}$ denoting the vector of the degrees of freedom associated to the velocity field and $\mathbf{P}^{(n,l)}$ denoting the vector of the degrees of freedom associated to the pressure.

Here, we have set

$$A_{ij}^{(n,l)} = \sum_{K\in\mathcal{T}_h}\int_K \rho^{(n,l)}\boldsymbol{\varphi}_j\cdot\boldsymbol{\varphi}_i d\Omega \tag{79}$$

$$B_{ij}^{(n,l)} = \sum_{K\in\mathcal{T}_h}\int_K -\tilde{a}_{ll}\frac{\Delta t}{M^2}\nabla\cdot\boldsymbol{\varphi}_i\Psi_j d\Omega + \sum_{\Gamma\in\mathcal{E}}\int_\Gamma \tilde{a}_{ll}\frac{\Delta t}{M^2}\left\{\{\Psi_j\}\right\}[[\boldsymbol{\varphi}_i]] \tag{80}$$

$$\begin{aligned}
F_i^{(n,l)} &= \sum_{m=1}^{l-1}\sum_{K\in\mathcal{T}_h}\int_K a_{lm}\Delta t\left(\rho^{(n,m)}\mathbf{u}^{(n,m)}\otimes\mathbf{u}^{(n,m)}\right):\nabla\boldsymbol{\varphi}_i d\Omega \\
&+ \sum_{m=1}^{l-1}\sum_{K\in\mathcal{T}_h}\int_K \tilde{a}_{lm}\frac{\Delta t}{M^2}p^{(n,m)}\nabla\cdot\boldsymbol{\varphi}_i d\Omega \\
&- \sum_{m=1}^{l-1}\sum_{\Gamma\in\mathcal{E}}\int_\Gamma a_{lm}\Delta t\left\{\left\{\rho^{(n,m)}\mathbf{u}^{(n,m)}\otimes\mathbf{u}^{(n,m)}\right\}\right\}:\langle\langle\boldsymbol{\varphi}_i\rangle\rangle\, d\Sigma \\
&- \sum_{m=1}^{l-1}\sum_{\Gamma\in\mathcal{E}}\int_\Gamma a_{lm}\Delta t\frac{\lambda^{(n,m)}}{2}\left\langle\left\langle\rho^{(n,m)}\mathbf{u}^{(n,m)}\right\rangle\right\rangle:\langle\langle\boldsymbol{\varphi}_i\rangle\rangle\, d\Sigma \\
&- \sum_{m=1}^{l-1}\sum_{\Gamma\in\mathcal{E}}\int_\Gamma \tilde{a}_{lm}\frac{\Delta t}{M^2}\left\{\left\{p^{(n,m)}\right\}\right\}[[\boldsymbol{\varphi}_i]]\, d\Sigma,
\end{aligned} \tag{81}$$

with $\boldsymbol{\varphi}_i$ and Ψ_i denoting the basis function of the space of polynomial functions employed to discretize the velocity and the pressure, respectively. Following the discussion in [46, 47], one can notice that we employ a centered flux for the quantities defined implicitly and upwind biased flux for the quantities computed explicitly. In order to obtain a numerical method effective for all Mach numbers, we take

$$\begin{aligned}
\lambda^{(n,m)} = \quad & \max\left[f\left(M_{loc}^{+,(n,m)}\right)\left(\left|\mathbf{u}^{+,(n,m)}\right|+\frac{1}{M}c^{+,(n,m)}\right),\right. \\
& \left. f\left(M_{loc}^{-,(n,m)}\right)\left(\left|\mathbf{u}^{-,(n,m)}\right|+\frac{1}{M}c^{-,(n,m)}\right)\right],
\end{aligned} \tag{82}$$

with $M_{loc}^{\pm,(n,m)} = \frac{|\mathbf{u}|^{\pm,(n,m)}}{\frac{1}{M}c^{\pm,(n,m)}}$ and $f\left(M_{loc}\right) = \min\left(1, M_{loc}\right)$. This choice corresponds to the convex combination between a centered flux and a Rusanov flux [50] discussed in [1]. More specifically, for a generic flux $\hat{\mathbf{F}}$, we employ

$$\hat{\mathbf{F}} = \left(1 - f\left(M_{loc}\right)\right)\mathbf{F}_c + f\left(M_{loc}\right)\mathbf{F}_R, \tag{83}$$

with $\mathbf{F}_c$ and $\mathbf{F}_R$ denoting the centered flux and the Rusanov flux, respectively. Hence, for $M_{loc}\approx 1$, we obtain the Rusanov flux, whereas for $M_{loc}\ll 1$, we obtain a local Lax-Friedrichs flux. Analogously, the energy equation in (58) can be expressed as

$$\mathbf{C}^{(n,l)}\mathbf{U}^{(n,l)} + \mathbf{D}^{(n,l)}\mathbf{P}^{(n,l)} = \mathbf{G}^{(n,l)}, \tag{84}$$

with

$$
\begin{aligned}
C_{ij}^{(n,l)} &= \sum_{K\in\mathcal{T}_h}\int_K -\tilde{a}_{ll}\Delta t h^{(n,l)}\rho^{n,l}\boldsymbol{\varphi_j}\cdot\nabla\Psi_i d\Omega \\
&+ \sum_{\Gamma\in\mathcal{E}}\int_\Gamma \tilde{a}_{ll}\Delta t\left\{\left\{h^{(n,l)}\rho^{(n,l)}\boldsymbol{\varphi_j}\right\}\right\}\cdot\nabla\Psi_i d\Sigma \qquad (85)\\
D_{ij}^{(n,l)} &= \sum_{K\in\mathcal{T}_h}\int_K \rho^{(n,l)}e^{(n,l)}(\Psi_j)\Psi_i d\Omega \qquad (86)\\
G_i^{(n,l)} &= \sum_{m=1}^{l-1}\sum_{K\in\mathcal{T}_h}\int_K \rho^{(n,l)}E^{(n,l)}\psi_i d\Omega \\
&+ \sum_{m=1}^{l-1}\sum_{K\in\mathcal{T}_h}\int_K a_{lm}\Delta t M^2\left(k^{(n,m)}\rho^{(n,m)}\mathbf{u}^{(n,m)}\right)\cdot\nabla\Psi_i d\Omega \\
&+ \sum_{m=1}^{l-1}\sum_{K\in\mathcal{T}_h}\int_K \tilde{a}_{lm}\Delta t\left(h^{(n,m)}\rho^{(n,m)}\mathbf{u}^{(n,m)}\right)\cdot\nabla\Psi_i d\Omega \\
&- \sum_{m=1}^{l-1}\sum_{\Gamma\in\mathcal{E}}\int_\Gamma a_{lm}\Delta t M^2\left\{\left\{k^{(n,m)}\rho^{(n,m)}\mathbf{u}^{(n,m)}\right\}\right\}\cdot[[\Psi_i]]\,d\Sigma \\
&- \sum_{m=1}^{l-1}\sum_{\Gamma\in\mathcal{E}}\int_\Gamma \tilde{a}_{lm}\Delta t\left\{\left\{h^{(n,m)}\rho^{(n,m)}\mathbf{u}^{(n,m)}\right\}\right\}\cdot[[\Psi_i]]\,d\Sigma \\
&- \sum_{m=1}^{l-1}\sum_{\Gamma\in\mathcal{E}}\int_\Gamma a_{lm}\Delta t\frac{\lambda^{(n,m)}}{2}\left[\left[\rho^{(n,m)}k^{(n,m)}\right]\right]\cdot[[\Psi_i]]\,d\Sigma \\
&- \sum_{m=1}^{l-1}\sum_{\Gamma\in\mathcal{E}}\int_\Gamma \tilde{a}_{lm}\Delta t\frac{\lambda^{(n,m)}}{2}\left[\left[\rho^{(n,m)}e^{(n,m)}\right]\right]\cdot[[\Psi_i]]\,d\Sigma. \qquad (87)
\end{aligned}
$$

Notice that, the upwind flux has been slightly modified with respect to the one employed in [47], so as to guarantee the preservation of uniform velocity and pressure fields (see the discussion in [46]). Formally, one can derive

$$
\mathbf{U}^{(n,l)} = \left(\mathbf{A}^{(n,l)}\right)^{-1}\left(\mathbf{F}^{(n,l)} - \mathbf{B}^{(n,l)}\mathbf{P}^{(n,l)}\right), \qquad (88)
$$

so as to obtain

$$
\mathbf{D}^{(n,l)}\mathbf{P}^{(n,l)} + \mathbf{C}^{(n,l)}\left(\mathbf{A}^{(n,l)}\right)^{-1}\left(\mathbf{F}^{(n,l)} - \mathbf{B}^{(n,l)}\mathbf{P}^{(n,l)}\right) = \mathbf{G}^{(n,l)}. \qquad (89)
$$

The above system can be solved following the fixed point procedure described in [19, 47]. More specifically, setting $\mathbf{P}^{(n,l,0)} = \mathbf{P}^{(n,l-1)}$, one solves for $L = 0,\dots,\tilde{L}$

$$
\left(\mathbf{D}^{(n,l,L)} - \mathbf{C}^{(n,l,L)}\left(\mathbf{A}^{(n,l)}\right)^{-1}\mathbf{B}^{(n,l)}\right)\mathbf{P}^{(n,l,L+1)} = \mathbf{G}^{(n,l,L)} - \mathbf{C}^{(n,l,L)}\left(\mathbf{A}^{(n,l)}\right)^{-1}\mathbf{F}^{(n,l,L)} \qquad (90)
$$

and then updates the velocity solving

$$
\mathbf{A}^{(n,l)}\mathbf{U}^{(n,2,L)} = \mathbf{F}^{(n,l,L)} - \mathbf{B}^{(n,l)}\mathbf{P}^{(n,l,L+1)}. \qquad (91)
$$

Notice that, as discussed for the time discretization in Section 3, the employed spatial discretization is not TVD for $r > 0$. A discussion of possible approaches to overcome this issue is out of the scope of the work. However, a number of approaches have been proposed to obtain essentially monotone schemes using high order DG methods, see e.g. [20, 45].

5 Numerical results

The analysis outlined in Sections 3 and 4 is now validated in a number of relevant benchmarks both for $M = O(1)$ and $M \ll 1$. The implementation is carried out in the framework of the *deal.II* library [2, 4]. The employed time discretization method is based on the second order IMEX scheme proposed in [24], for which the coefficients are reported in the Butcher tableaux Table 1 and Table 2 for the explicit and implicit method, respectively.

0	0		
χ	χ	0	
1	$1 - a_{32}$	a_{32}	0
	$\frac{1}{2} - \frac{\chi}{4}$	$\frac{1}{2} - \frac{\chi}{4}$	$\frac{\chi}{2}$

Table 1: *Butcher tableau of the explicit ARK2 method*

0	0		
χ	$\frac{\chi}{2}$	$\frac{\chi}{2}$	
1	$\frac{1}{2\sqrt{2}}$	$\frac{1}{2\sqrt{2}}$	$1 - \frac{1}{\sqrt{2}}$
	$\frac{1}{2} - \frac{\chi}{4}$	$\frac{1}{2} - \frac{\chi}{4}$	$\frac{\chi}{2}$

Table 2: *Butcher tableau of the implicit ARK2 method*

We consider $\chi = 2-\sqrt{2}$, so that the implicit part of the IMEX scheme coincides with the TR-BDF2 method [5, 35]. Notice also that, as discussed in [47], we take $a_{32} = 0.5$, rather than the value originally chosen in [24], so as to improve the monotonicity of the method. We set

$$\mathcal{H} = \min \{\text{diam}\,(K)\,|K \in \mathcal{T}_h\} \tag{92}$$

and we define two Courant numbers, one based on the speed of sound denoted by C, the so-called acoustic Courant number, and one based on the local velocity of the flow, the so-called advective Courant number, denoted by C_u:

$$C = \frac{1}{M} rc \frac{\Delta t}{\mathcal{H}} \qquad C_u = ru \frac{\Delta t}{\mathcal{H}}, \tag{93}$$

where c is the speed of sound and u is the magnitude of the flow velocity. For the tests using the ideal gas law (9), $\gamma = 1.4$ is employed.

5.1 Colliding acoustic pulses

This benchmark, proposed in [38], consists of two colliding acoustic pulses in the domain $\Omega = (-L, L)$, namely, a right-running pulse initially located in $(-L, 0)$ and a left-running pulse initially located in $(0, L)$. Following [38], we set $M = \frac{1}{11}$ and we define the half-length of the domain $L = \frac{2}{M} = 22$. Periodic boundary conditions are prescribed. The initial conditions read as follows:

$$\rho(x,0) = \bar{\rho}_0 + \frac{1}{2} M \rho_0^{'} \left(1 - \cos\left(\frac{2\pi x}{L}\right)\right) \qquad \bar{\rho}_0 = 0.955 \quad \rho_0^{'} = 2 \tag{94}$$

$$u(x,0) = -\frac{1}{2}\,\mathrm{sgn}(x)\,\bar{u}_0 \left(1 - \cos\left(\frac{2\pi x}{L}\right)\right) \quad \bar{u}_0 = 2\sqrt{\gamma} \tag{95}$$

$$p(x,0) = \bar{p}_0 + \frac{1}{2} M p_0^{'} \left(1 - \cos\left(\frac{2\pi x}{L}\right)\right) \qquad \bar{p}_0 = 1 \quad p_0^{'} = 2\gamma \tag{96}$$

The final time is $T_f = 1.63$. We consider a number of elements $N_{el} = 110$ with $r = 1$, i.e. polynomial degree of order 1, whereas the time step is $\Delta t = 0.0163$, leading to a maximum advective Courant number $C_u \approx 0.1$ and a maximum acoustic Courant number $C \approx 0.56$. The pressure profiles at $t = \frac{T_f}{2} = 0.815$ and $t = T_f$ are in agreement with the results present in the literature [16, 38, 44] (Figure 1). One can easily notice that at $t = \frac{T_f}{2}$, the two pulses are superposed and the pressure reaches its maximum value. At $t = T_f$, the pulses are separated from each other and assume almost the initial configuration. However, as explained in [16, 38], weakly non-linear acoustic effects start steepening the pulses and distort the final profile, since shocks are beginning to form around $x = \pm 18.5$.

5.2 Density layering

We consider now the test case II proposed in [38] and described also e.g. in [44]. The domain is $\Omega = (-L, L)$, with $L = \frac{1}{0.02} = 50$. The initial conditions read as follows:

$$\rho(x,0) = \bar{\rho}_0 + \Phi(x)\,\tilde{\rho}_0 \sin\left(\frac{40\pi x}{L}\right) + \frac{1}{2} M \rho_1 \left(1 + \cos\left(\frac{\pi x}{L}\right)\right) \tag{97}$$

$$u(x,0) = \frac{1}{2}\tilde{u}_0 \left(1 + \cos\left(\frac{\pi x}{L}\right)\right) \tag{98}$$

$$p(x,0) = \bar{p}_0 + \frac{1}{2} M p_1 \left(1 + \cos\left(\frac{\pi x}{L}\right)\right), \tag{99}$$

with $\bar{\rho}_0 = 1, \tilde{\rho}_0 = \frac{1}{2}, \rho_1 = 2, \tilde{u}_0 = 2\sqrt{\gamma} = 2\sqrt{1.4}, \bar{p}_0 = 1$, and $p_1 = 2\gamma = 2.8$. Finally, the function $\Phi(x)$ is given by

$$\Phi(x) = \begin{cases} \frac{1}{2}\left(1 - \cos\left(\frac{5\pi x}{L}\right)\right) & \text{if } 0 \le x \le \frac{2}{5}L \\ 0 & \text{otherwise.} \end{cases} \tag{100}$$

The initial data describe a density layering of large amplitude and small wavelengths, which is driven by the motion of a right-moving periodic acoustic wave with long wavelength. Periodic boundary conditions are prescribed. The final time is $T_f = 5.071$. We consider a computational grid composed by $N_{el} = 500$ elements with $r = 1$, whereas

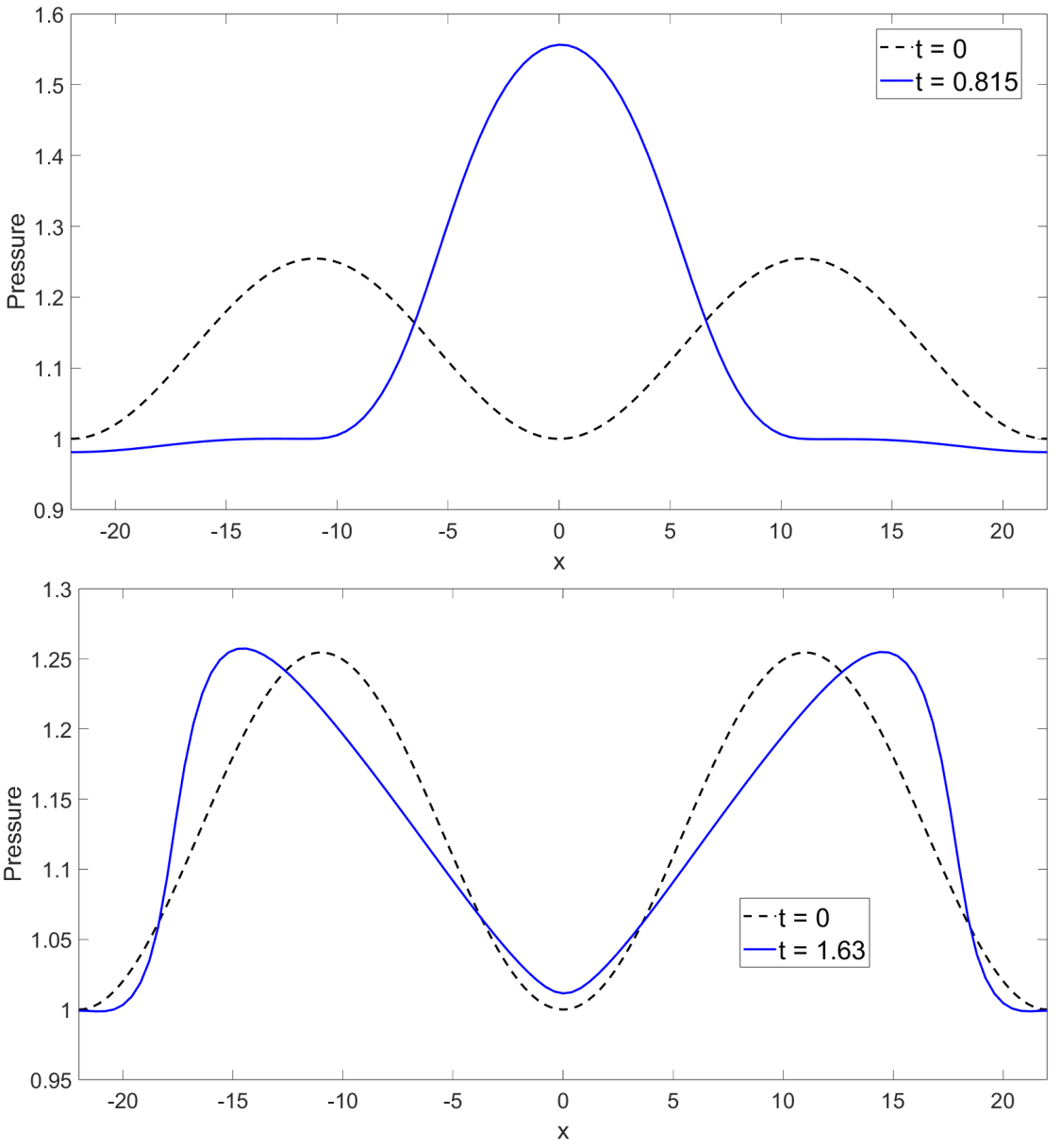

Figure 1: Colliding acoustic pulses test case, pressure profile. Top: $t = \frac{T_f}{2}$. Bottom: $t = T_f$. The initial profile is in dashed black line, whereas the solid blue line provides the results at the corresponding time.

the time step is $\Delta t = 0.025355$. Following [44], we start considering $M = \frac{1}{50}$. Hence, the advective Courant C_u is around 0.3, while the acoustic Courant number C is around 10.5. A comparison between the initial and the final time for both the density and the pressure displays a good agreement with the results presented in [38, 44] (Figure 2). One can easily notice that the acoustic wave transports the density layer and the shape of the layer is undistorted. As in the previous test case, due to weakly non-linear effects, the pulse starts steepening, leading to shock formation. A reference solution has been computed using the explicit second order strong stability preserving

(SSP) scheme described in [25], to which we refer for all the details. The time step employed for the explicit scheme is $\Delta t = 0.00025355$, namely 100 times smaller than that used with the IMEX scheme. An excellent agreement is established between the two solutions.

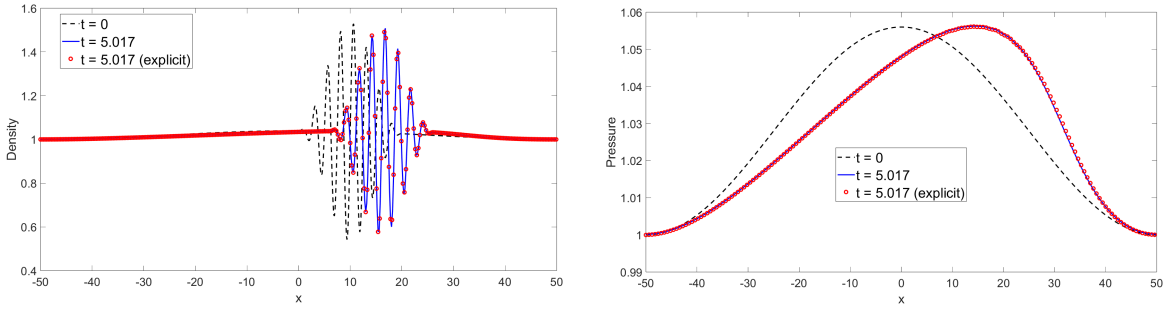

Figure 2: Density layering test case at $M = 0.02$ with the ideal gas law (9). Left: density. Right: pressure. The dashed black line represents the initial condition, the continuous blue line shows the solution at the final time, whereas the red dots report the solution obtained with the second order optimal explicit SSP scheme.

For the sake of completeness, we also consider a case even closer to the incompressible regime, taking $M = 10^{-4}$. The analytical solution of the leading order term of the limiting model (49) with initial conditions (97)-(99) is

$$\rho = \bar{\rho}_0 + \Phi\left(x - \bar{u}\left(t\right)t\right)\tilde{\rho}_0 \sin\left(\frac{40\pi\left(x - \bar{u}\left(t\right)t\right)}{L}\right) \tag{101}$$

$$u = \bar{u}\left(t\right) \tag{102}$$

$$p = \bar{p}_0, \tag{103}$$

$\bar{u}\left(t\right)$ being a function only of time. Since we are considering periodic boundary conditions, the value of $\bar{u}$ is not fixed a priori. The steady value of $\bar{u}$ obtained with the numerical simulation is the mean value of (98), namely $\bar{u} = \frac{1}{2}\tilde{u}_0 = \sqrt{\gamma} = \sqrt{1.4}$. A comparison at $t = T_f$ between the analytical solution as $M \to 0$ with $\bar{u} = \sqrt{\gamma} = \sqrt{1.4}$ and the numerical results shows an excellent agreement for both the density and the pressure profile (Figure 3). Notice that the initial velocity field is not divergence-free, namely it is not well-prepared. However, the numerical method leads to the incompressible limit, as already discussed in Section 2.2.

We now consider a configuration of this test case for the SG-EOS (10). We take $\gamma = 4.4, \pi_\infty = 6.8 \times 10^{-3}$, and $q_\infty = 0$ in (10). Notice that, we do not modify the initial conditions (97)-(99), namely we keep $\tilde{u}_0 = 2\sqrt{1.4}$ and $p_1 = 2.8$. We start considering $M = \frac{1}{50} = 0.02$. The time step is now $\Delta t = 0.020284$, yielding an acoustic Courant number $C \approx 15$ and a maximum advective Courant number $C_u \approx 0.24$. Figure 4 shows a comparison between the initial and the final time for both the density and the pressure. A reference solution has been computed using the second order explicit SSP scheme, with a time step $\Delta t = 0.000126775$, namely a time step 160 times smaller than that employed with the IMEX scheme. One can easily notice that the density layer is transported without too much damping. Moreover, a reasonable agreement with the explicit solution is established. Finally, for what concerns the incompressible limit at

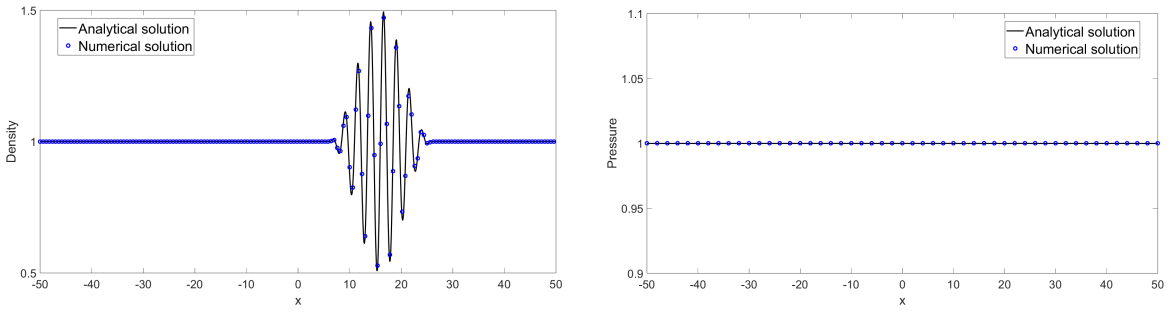

Figure 3: Density layering test case at $M = 10^{-4}$ with the ideal gas law (9). Left: density. Right: pressure. The continuous black line represents the analytical solution of the limiting model (49), while the blue dots report the numerical results.

$M = 10^{-4}$, since $\frac{\partial \bar{p}_0}{\partial t} = 0$, all the equations of state lead to the same limit (see (38)). This is further confirmed by the density and pressure profiles reported in Figure 5.

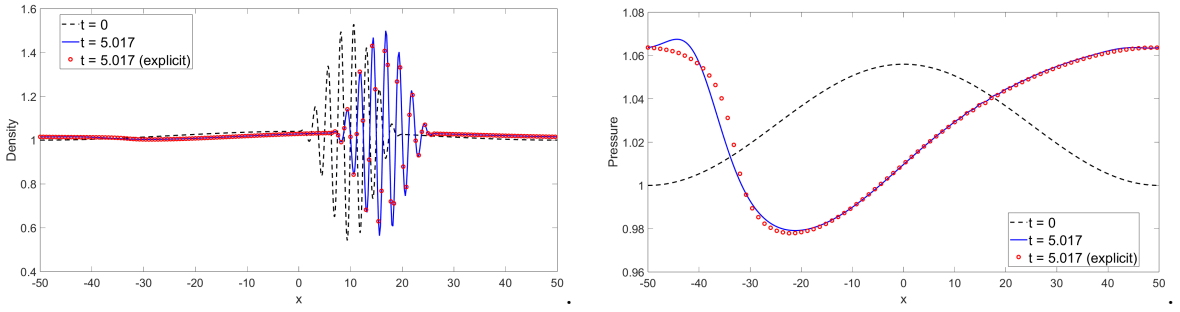

Figure 4: Density layering test case at $M = 0.02$ with the SG-EOS (10). Left: density. Right: pressure. The dashed black line represents the initial condition, the continuous blue line shows the solution at the final time, whereas the red dots report the solution obtained with the second order optimal explicit SSP scheme.

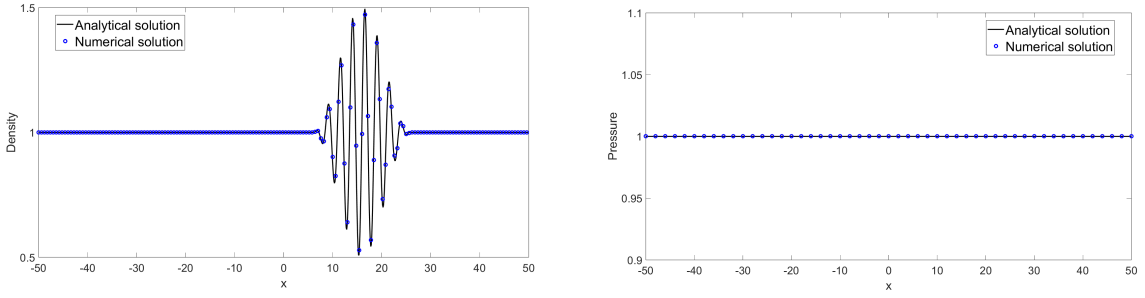

Figure 5: Density layering test case at $M = 10^{-4}$ with the SG-EOS (10). Left: density. Right: pressure. The continuous black line represents the analytical solution of the limiting model (49), while the blue dots report the numerical results.

5.3 Flow in an open tube

We consider now the test case III proposed in [38] for an ideal gas, which we recall here for the convenience of the reader. A flow in an open tube represented by the domain $\Omega = (0, 10)$ is analyzed; at the left-end a time dependent density and velocity are prescribed, whereas at the right-end a time dependent outflow pressure with large amplitude variation is imposed. More specifically, the initial conditions read as follows:

$$(\rho, u, p)(x, 0) = (1, 1, 1), \tag{104}$$

while the boundary conditions are

$$\rho(0, t) = 1 + \frac{3}{10}\sin(4t) \tag{105}$$

$$u(0, t) = 1 + \frac{1}{2}\sin(2t) \tag{106}$$

$$p(L, t) = 1 + \frac{1}{4}\sin(3t), \tag{107}$$

with $L = 10$. The final time is $T_f = 7.47$. The Mach number is set to $M = 10^{-4}$. We consider a number of elements $N_{el} = 100$ with $r = 1$, whereas the time step is $\Delta t = 0.0018675$, leading to a maximum advective Courant number $C_u \approx 0.13$ and a maximum acoustic Courant number $C \approx 310$. The results at $t = T_f$ are those expected by the asymptotic analysis for both the density and velocity profile (Figure 6). The limit solution as $M \to 0$ has been included for comparison in Figure 6. For an ideal gas, (33) reduces to

$$\nabla \cdot \bar{\mathbf{u}} = -\frac{1}{\gamma \bar{p}} \frac{\partial \bar{p}}{\partial t} = -\frac{1}{\gamma \bar{p}} \frac{d\bar{p}}{dt}, \tag{108}$$

since $\nabla \bar{p} = \mathbf{0}$. Hence, for $M \to 0$, in one space dimension, $\frac{\partial \bar{\mathbf{u}}}{\partial x}$ is a function only of time and, therefore, the velocity is a linear function of space with a given time dependent slope and boundary value at $x = 0$. For what concerns the density, we rewrite (24) as follows:

$$\frac{\partial \bar{\rho}}{\partial t} + \bar{\mathbf{u}} \cdot \nabla \bar{\rho} + \bar{\rho} \nabla \cdot \bar{\mathbf{u}} = \frac{\partial \bar{\rho}}{\partial t} + \bar{\mathbf{u}} \cdot \nabla \bar{\rho} - \frac{1}{\gamma} \frac{\bar{\rho}}{\bar{p}} \frac{d\bar{p}}{dt} = 0, \tag{109}$$

or, equivalently,

$$\frac{D \log \bar{\rho}}{Dt} = \frac{1}{\gamma} \frac{d \log \bar{p}}{dt}, \tag{110}$$

with $\frac{D}{Dt} = \frac{\partial}{\partial t} + \mathbf{u} \cdot \nabla$ denoting the Lagrangian derivative. Hence, as discussed in [38], the material elements undergo a quasi-static adiabatic compression and expansion following the particle paths described by $\bar{u}$. One can easily notice from the density profile in Figure 6 that mass elements, after entering the domain at the left-end, are correctly compressed and expanded.

We consider now an extension of this test case for the SG-EOS (10). Equation (33) reduces to

$$\nabla \cdot \bar{\mathbf{u}} = -\frac{1}{\gamma (\bar{p} + \pi_\infty)} \frac{d\bar{p}}{dt}. \tag{111}$$

Hence, the velocity is still a linear function of space with a different time dependent slope with respect to that of the ideal gas. Analogous considerations hold for the

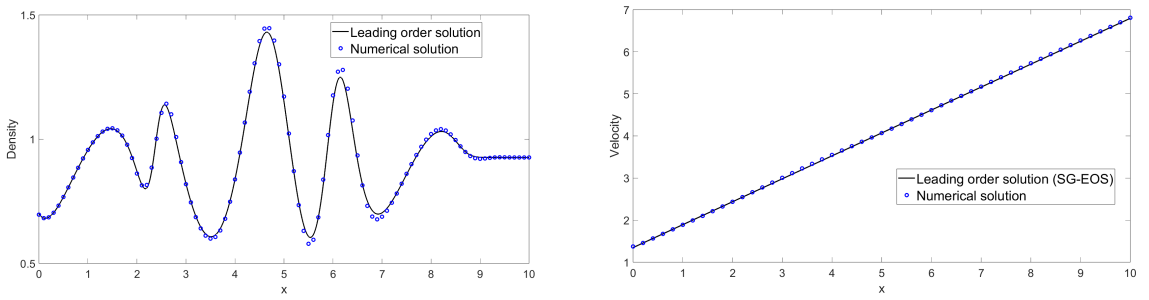

Figure 6: Open tube test case with the ideal gas law (9), results at $t = T_f = 7.47$. Left: density. Right: velocity. The continuous black line shows the leading order solution as $M \to 0$, whereas the blue dots report the numerical results.

continuity equation, which reduces to

$$\frac{D \log \bar{\rho}}{Dt} = \frac{1}{\gamma \left(\bar{p} + \pi_\infty\right)} \frac{d\bar{p}}{dt} = \frac{1}{\gamma} \frac{d \log \left(\bar{p} + \pi_\infty\right)}{dt}. \tag{112}$$

We take $\gamma = 4.4, \pi_\infty = 6.8 \times 10^{-3}$, and $q_\infty = 0$ in (10). We consider $\Delta t = 0.001245$. Hence, the maximum advective Courant number is $C_u \approx 0.04$, while the maximum acoustic Courant number is $C \approx 350$. A comparison at the final time between the numerical results and the leading order solution for both the density and the velocity displays a good agreement for both profiles (Figure 7). The leading order term solution as $M \to 0$ for the ideal gas has been included in Figure 7. One can easily notice a visible difference in the behaviour of both density and velocity. Hence, if large amplitude pressure variations are considered, the limiting regime depends on the equation of state and does not correspond to the incompressible Euler equations.

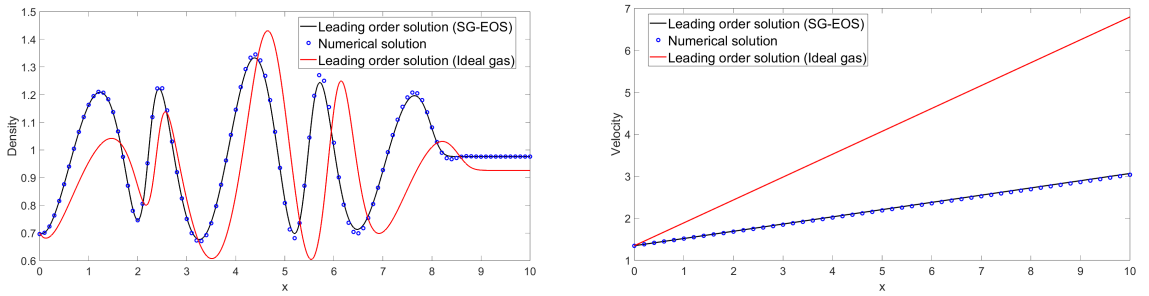

Figure 7: Open tube test case with the SG-EOS (10), results at $t = T_f = 7.47$. Left: density. Right: velocity. The continuous black line shows the leading order solution as $M \to 0$, the blue dots report the numerical results, while the red line shows the leading order solution as $M \to 0$ with the ideal gas.

Finally, we consider the Peng-Robinson EOS (14). The asymptotic analysis becomes much more involved. First of all, notice that

$$\frac{\partial \bar{\rho}\bar{e}}{\partial \bar{p}} = \frac{1 - \bar{\rho} b}{\gamma - 1}. \tag{113}$$

Moreover, we get

$$\frac{\partial \bar{h}}{\partial \bar{\rho}} = -\frac{\gamma}{\gamma - 1} \frac{\bar{p}}{\bar{\rho}^2} + g\left(\bar{\rho}\right), \tag{114}$$

with

$$g(\bar{\rho}) = \frac{a(1-2\bar{\rho}b)}{(\gamma-1)(1-\bar{\rho}br_1)(1-\bar{\rho}br_2)} + \frac{ab\bar{\rho}(1-\bar{\rho}b)(r_1(1-\bar{\rho}br_2)+r_2(1-\bar{\rho}br_1))}{(\gamma-1)(1-\bar{\rho}br_1)^2(1-\bar{\rho}br_2)^2} + \frac{a}{b}\frac{\partial U}{\partial \bar{\rho}}. \quad (115)$$

Hence, (33) reduces to

$$\left(-\frac{\gamma}{\gamma-1}\bar{p}+\bar{\rho}^2 g(\bar{\rho})\right)\nabla\cdot\bar{\mathbf{u}} = \frac{1-\bar{\rho}b}{\gamma-1}\frac{d\bar{p}}{dt}, \quad (116)$$

or, equivalently, to

$$\nabla\cdot\bar{\mathbf{u}} = -\frac{1-\bar{\rho}b}{\gamma\bar{p}-(\gamma-1)\bar{\rho}^2 g(\bar{\rho})}\frac{d\bar{p}}{dt}. \quad (117)$$

Notice that, $\nabla\cdot\bar{\mathbf{u}}$ is now a function of both space and time. Hence, in one space dimension, the velocity is no longer a linear profile. The continuity equation (24) reads as follows:

$$\frac{D\log\bar{\rho}}{Dt} = -\nabla\cdot\bar{\mathbf{u}} = \frac{1-\bar{\rho}b}{\gamma\bar{p}-(\gamma-1)\bar{\rho}^2 g(\bar{\rho})}\frac{d\bar{p}}{dt}. \quad (118)$$

We take $\gamma = 1.4, a = 1$, and $b = 0.15$. The time step is $\Delta t = 0.0018675$, yielding a maximum advective Courant number $C_u \approx 0.13$ and a maximum acoustic Courant number $C \approx 300$. A comparison at the final time between the numerical results and the leading order solution for both the density and the velocity shows a good agreement for both profiles (Figure 13). The results are similar to those obtained with the ideal gas. Weakly non-ideal gas effects are present in particular between $x = 4$ and $x = 6$, namely in correspondence of the peak density.

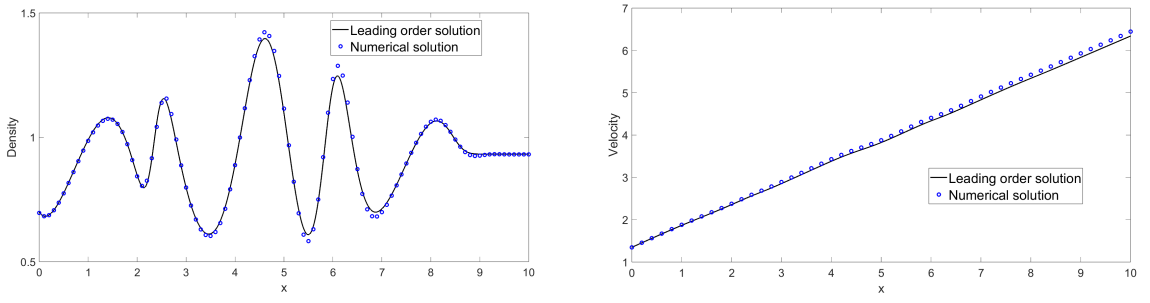

Figure 8: Open tube test case with the Peng-Robinson EOS (14), results at $t = T_f = 7.47$. Left: density. Right: velocity. The continuous black line shows the leading order solution as $M \to 0$, the blue dots report the numerical results.

5.4 Gresho vortex

In this Section, we perform simulations of the so-called Gresho vortex [27, 43], which is a stationary solution of the incompressible Euler equations. The centrifugal force, indeed, is balanced by the gradient of the pressure. A rotating vortex is positioned at

the center $(0.5, 0.5)$ of the computational domain $\Omega = (0,1)^2$. The initial conditions for dimensional variables read as follows:

$$\rho(x,0) = 1 \tag{119}$$

$$u(x,0) = -u_\varphi \sin(\varphi) \tag{120}$$

$$v(x,0) = u_\varphi \cos(\varphi) \tag{121}$$

$$p(x,0) = \begin{cases} p_0 + \frac{25}{2}\rho r^2 & \text{if } 0 \le r < 0.2 \\ p_0 + \frac{25}{2}\rho r^2 + 4\rho(1 - 5r - \log(0.2) + \log(r)) & \text{if } 0.2 \le r < 0.4 \\ p_0 - \rho(2 - 4\log(2)) & \text{if } r \ge 0.4. \end{cases} \tag{122}$$

Here, $r = \sqrt{(x-0.5)^2 + (y-0.5)^2}, \varphi = \arctan\left(\frac{y-0.5}{x-0.5}\right), p_0 = \frac{\rho_0 u_{\varphi,max}^2}{\gamma M^2}$, with $\rho_0 = 1\,\mathrm{kg\,m^{-3}}$ and $u_{\varphi,max} = 1\,\mathrm{m\,s^{-1}}$ for $r = 0.2$. Finally, u_φ is

$$u_\varphi = \begin{cases} 5r & \text{if } 0 \le r < 0.2 \\ 2 - 5r & \text{if } 0.2 \le r < 0.4 \\ 0 & \text{if } r \ge 0.4. \end{cases} \tag{123}$$

Notice that, as discussed in [29], the pressure p_0 is chosen in such a way that the maximum value of $\frac{|\mathbf{u}|}{c}$ matches M, so as to consider low Mach effects. We transform the initial conditions in non-dimensional quantities by using $\mathcal{R} = 1\,\mathrm{kg\,m^{-3}}, \mathcal{L} = 1\,\mathrm{m}$, and $\mathcal{U} = 1\,\mathrm{m\,s^{-1}}$. Periodic boundary conditions are imposed for all the boundaries. We simulate the flow until $T_f = 3$, when three full rotations are completed. The computational grid is composed by 80×80 elements with polynomial degree $r = 2$, whereas the time step is $\Delta t = 0.002$, leading an advective Courant number $C_u \approx 0.32$. We consider $M = 10^{-3}$ and $M = 10^{-4}$. Hence, the acoustic Courant number is $C \approx 320$ for $M = 10^{-3}$ and $C \approx 3200$ for $M = 10^{-4}$. A comparison of the local Mach number $M_{loc} = \frac{M|\mathbf{u}|}{c}$ at initial time and the final time for the two tests shows that the numerical method accurately preserves the shape of the vortex (Figure 9). We also monitor the behaviour over time of the kinetic energy, which should be conserved. Figure 10 shows the behaviour over the time of the relative difference of the kinetic energy with respect to the initial value, namely $\frac{|E_{kin}(t) - E_{kin}(0)|}{E_{kin(0)}}$, for $M = 10^{-3}$. Table 3 reports instead the total kinetic energy relative to the initial one after each rotation. The kinetic energy is conserved and these results compare very well with those presented in [1], [56] where a loss of about 1.5 percent of the initial kinetic energy occurs after one rotation of the vortex. Analogous results are achieved for $M = 10^{-4}$. Hence, the preservation of the kinetic energy holds independently of the Mach number.

M	$t = 1$	$t = 2$	$t = 3$
10^{-3}	0.999981	0.999974	0.999968
10^{-4}	0.999981	0.999974	0.999969

Table 3: Total kinetic energy relative to its initial value for different Mach numbers after each full rotation of the Gresho vortex with the ideal gas law (9).

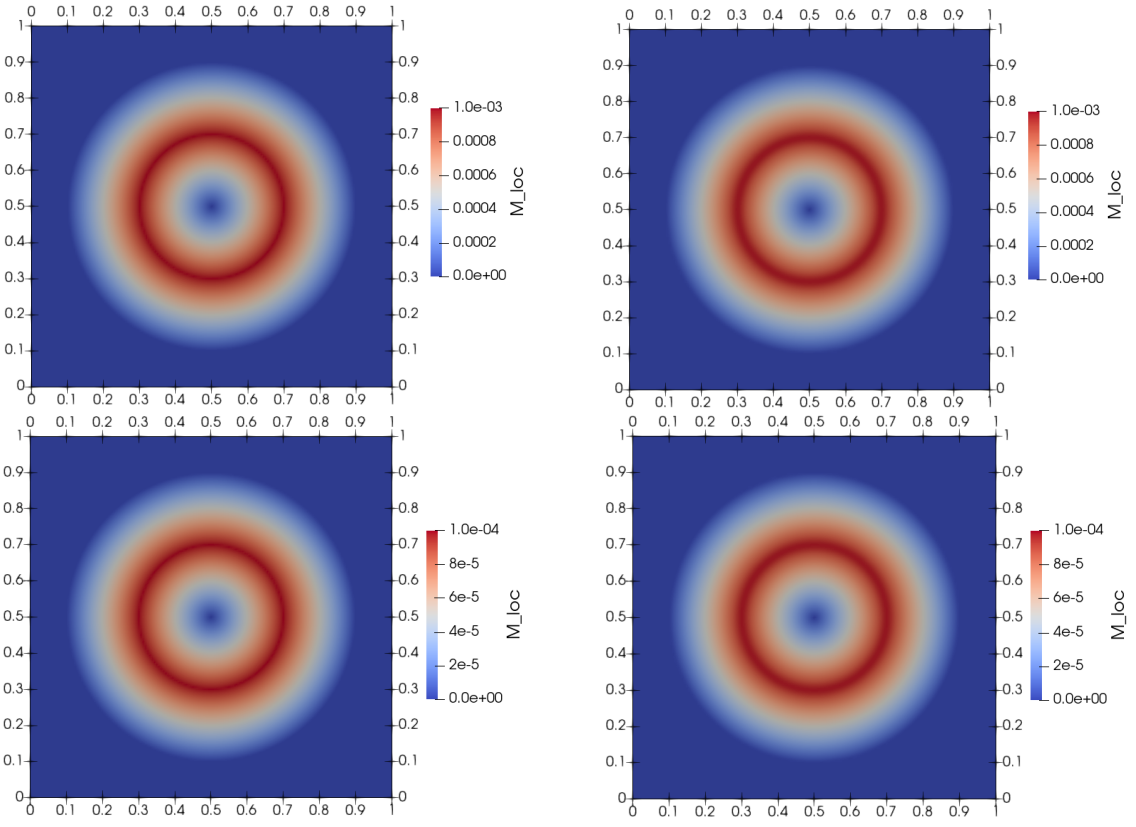

Figure 9: Gresho vortex test case with the ideal gas law (9), comparison of local Mach number $M_{loc} = \frac{M|\mathbf{u}|}{c}$. From bottom to top: results at $M = 10^{-4}$ and $M = 10^{-3}$. From left to right: initial condition and results at $t = T_f = 3$, after three full rotations.

We now adapt the standard Gresho vortex test case to a water flow. As discussed in [1], it suffices to modify p_0 for the SG-EOS (10) as follows:

$$p_0 = \frac{\rho_0 u_{\varphi,max}^2}{\gamma M^2} - \pi_\infty, \tag{124}$$

with $M = 10^{-4}, \rho_0 = 1000\,\mathrm{kg\,m^{-3}}, \gamma = 4.4$, and $\pi_\infty = 6.8 \times 10^8\,\mathrm{Pa}$. We also take $q_\infty = 0$ in (10). The initial density is now $\rho(x,0) = \rho_0$ and we employ $\mathcal{R} = 1000\,\mathrm{kg\,m^{-3}}$ to compute the non-dimensional counter part of initial conditions (119)-(122). A comparison of M_{loc} between the initial and the final time shows that the shape of the vortex is accurately preserved also for a fluid with parameters corresponding to those of water (Figure 11). Figure 12 shows the behaviour over the time of the relative difference of the kinetic energy with respect to the initial value, while Table 4 reports the total kinetic energy relative to the initial one after each rotation, from which we notice that the kinetic energy is conserved.

Finally, we consider a configuration of the Gresho vortex for the Peng-Robinson EOS (14). The new expression of the background pressure p_0 reads as follows:

$$p_0 = \left[\frac{u_{\varphi,max}^2}{M^2} + f(\rho_0)\right] \frac{\rho_0(1-\rho_0 b)}{\gamma}, \tag{125}$$

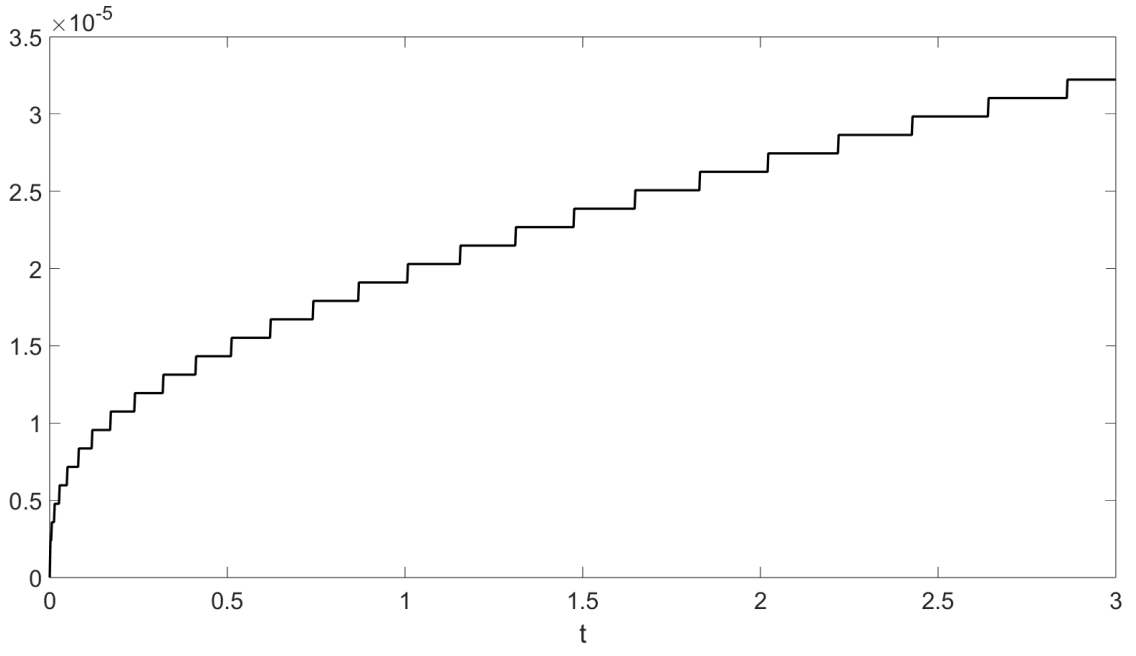

Figure 10: Gresho vortex test case with the ideal gas law (9), relative difference of the total kinetic energy with respect to the initial value at $M = 10^{-3}$.

M	$t = 1$	$t = 2$	$t = 3$
10^{-4}	0.999981	0.999974	0.999968

Table 4: Total kinetic energy relative to its initial value after each full rotation of the Gresho vortex with the SG-EOS (10).

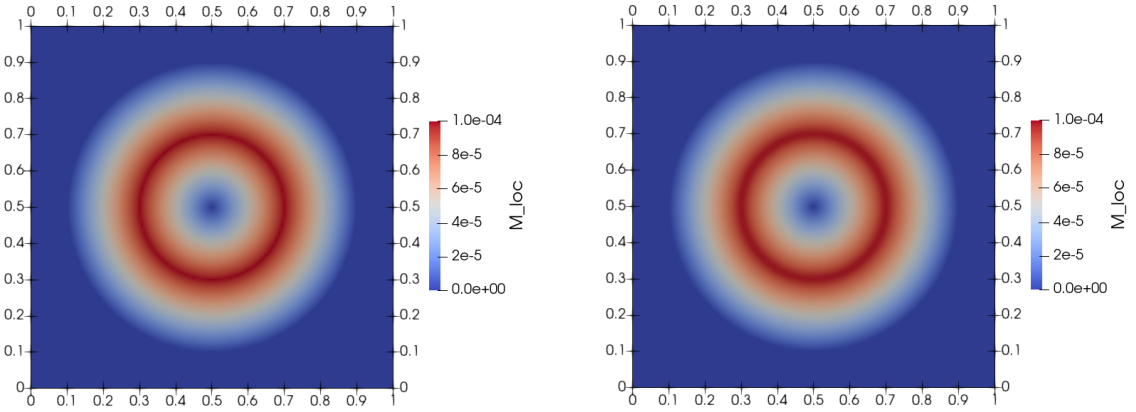

Figure 11: Gresho vortex test case with SG-EOS (10), comparison of local Mach number $M_{loc} = \frac{M|\mathbf{u}|}{c}$. Left: initial condition. Right: results at $t = T_f = 3$, after three full rotations.

with

$$f(\rho_0) = \frac{a\rho_0}{1-\rho_0 b}\left(\frac{\frac{\partial U}{\partial \rho_0}}{b}(\gamma-1)+\frac{1-2\rho_0 b}{(1-\rho_0 b r_1)(1-\rho_0 b r_2)}\right) + ab\rho_0^2\frac{r_1(1-\rho_0 b r_2)^2+r_2(1-\rho_0 b r_1)}{(1-\rho_0 b r_1)^2(1-\rho_0 b r_2)^2}. \quad (126)$$

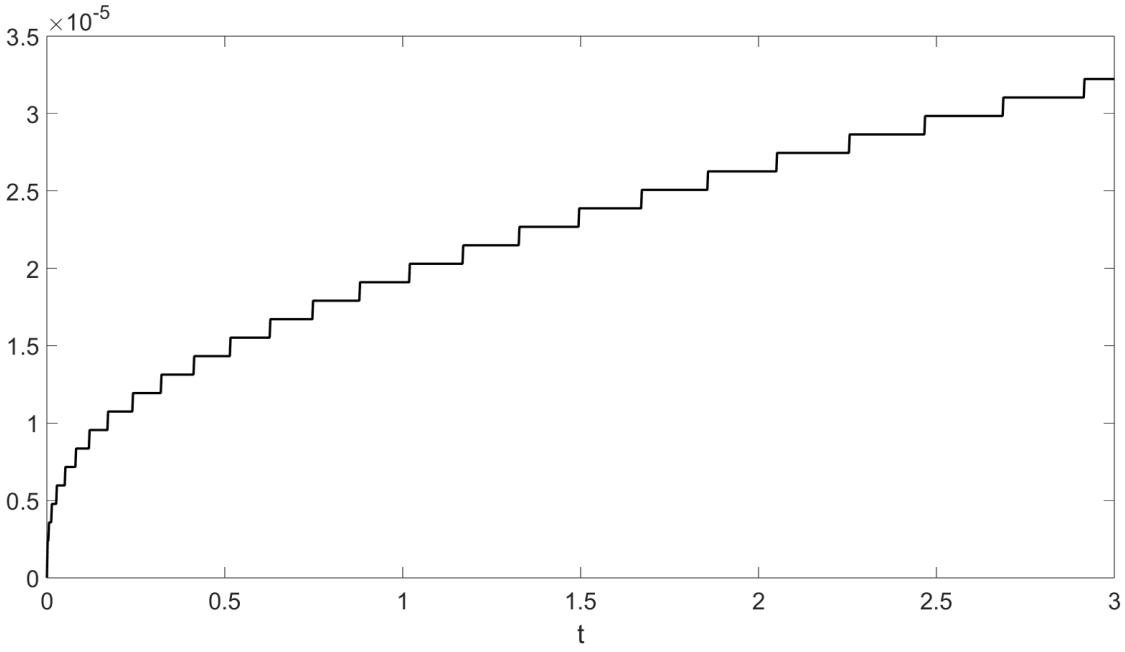

Figure 12: Gresho vortex test case with SG-EOS (10), relative difference of the total kinetic energy with respect to the initial value at $M = 10^{-4}$.

We take $\gamma = 1.4, \rho_0 = 1\,\mathrm{kg\,m^{-3}}, a = 500\,\mathrm{m^5\,s^{-2}\,kg^{-1}}$, and $b = 0.001\,\mathrm{m^3\,kg^{-1}}$. Finally, we consider $\rho(x, 0) = 1\,\mathrm{kg\,m^{-3}}$ and this value is also employed to compute non-dimensional quantities. Figure 13 shows a comparison of M_{loc} between the initial and the final time, Figure 14 shows the behaviour over the time of the relative difference of the kinetic energy with respect to the initial value, while Table 5 reports the total kinetic energy relative to the initial one after each rotation. The same considerations done for the ideal gas law (9) and for the SG-EOS (10) are valid also for this particularly challenging and complex equation of state.

M	$t = 1$	$t = 2$	$t = 3$
10^{-4}	0.999981	0.999974	0.999969

Table 5: Total kinetic energy relative to its initial value after each full rotation of the Gresho vortex with the Peng-Robinson EOS (14).

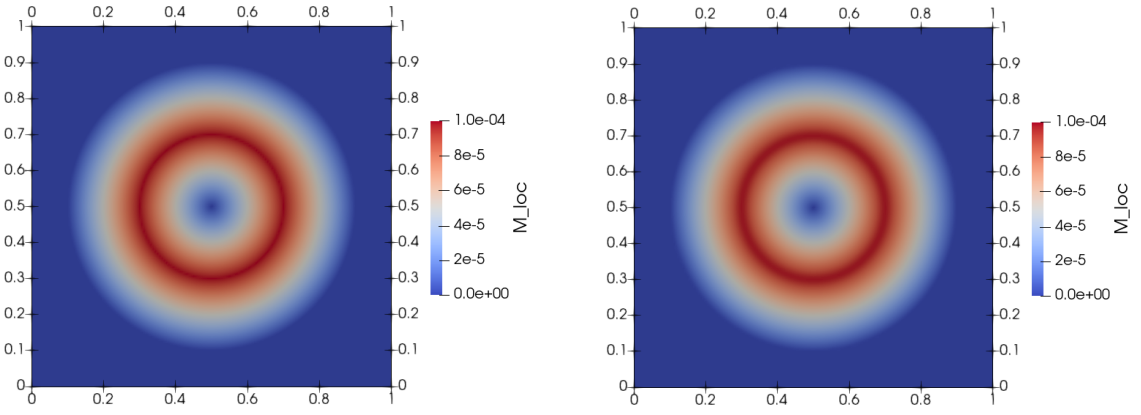

Figure 13: Gresho vortex test case with the Peng-Robinson EOS (14), comparison of local Mach number $M_{loc} = \frac{M|\mathbf{u}|}{c}$. Left: initial condition. Top: results at $t = T_f = 3$, after three full rotations.

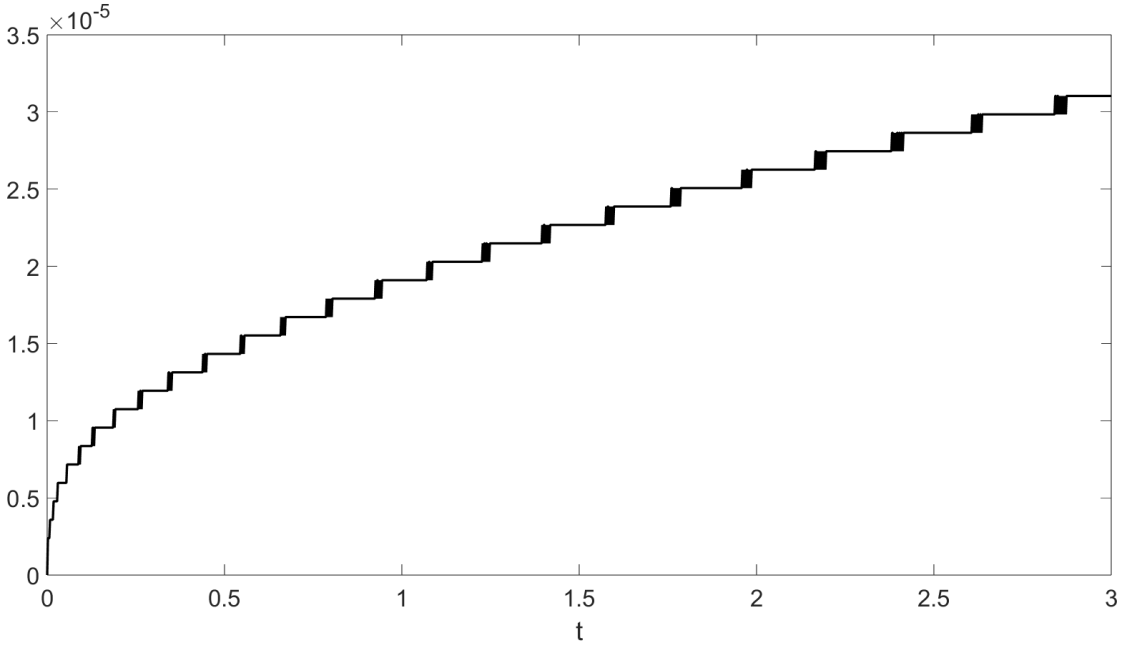

Figure 14: Gresho vortex test case with the Peng-Robinson EOS (14), relative difference of the total kinetic energy with respect to the initial value at $M = 10^{-4}$.

5.5 Baroclinic vorticity generation problem

We now consider a test case proposed in [22] and discussed also in [39, 44], which consists of a right-going acoustic wave crossing a density fluctuation in the vertical direction. The ideal gas law (9) is employed. The computational domain is $\Omega = (-L, L) \times \left(0, \frac{2}{5}L\right)$. Following [39, 44], we set $M = 5 \times 10^{-2}$ and we take $L = \frac{1}{M}$. The

initial conditions read as follows:

$$\bar{\rho}\left(\mathbf{x},0\right) = \bar{\rho}_0 + M\rho_0^{'}\left(1+\cos\left(\frac{\pi x}{L}\right)\right) + \Phi\left(y\right) \tag{127}$$

$$u\left(\mathbf{x},0\right) = \bar{u}_0\left(1+\cos\left(\frac{\pi x}{L}\right)\right) \tag{128}$$

$$v\left(\mathbf{x},0\right) = 0 \tag{129}$$

$$p\left(\mathbf{x},0\right) = \bar{p}_0 + Mp_0^{'}\left(1+\cos\left(\frac{\pi x}{L}\right)\right), \tag{130}$$

with $\bar{\rho}_0 = 1, \rho_0^{'} = 0.2, \bar{p}_0 = 1.p_0^{'} = \gamma$, and $\bar{u}_0 = \sqrt{\gamma}$. The function $\Phi\left(y\right)$ is defined by

$$\Phi\left(y\right) = \begin{cases} \rho_2 \frac{y}{\frac{2}{5}L} & \text{if } y \leq \frac{1}{5}L - \varepsilon \\ \rho_2\left(\frac{y}{\frac{2}{5}L} - \frac{1}{2}\right) - 0.4 & \text{if } y \geq \frac{1}{5}L + \varepsilon \\ \rho_2 \frac{\frac{1}{5}L-\varepsilon}{\frac{2}{5}L} + \frac{1}{2\varepsilon}\left(\rho_2\left(\frac{\frac{1}{5}L+\varepsilon}{\frac{2}{5}L} - \frac{1}{2}\right) - 0.4 - \rho_2\frac{\frac{1}{5}L-\varepsilon}{\frac{2}{5}L}\right)\left(y - \frac{1}{5}L + \varepsilon\right) & \text{otherwise,} \end{cases}$$

where $\rho_2 = 0.8$ and $\varepsilon = 0.01$. Notice that, unlike in [39, 44], the function Φ is regularized to obtain a continuous profile. Periodic boundary conditions are prescribed, whereas the final time is $T_f = 16$. The computational grid is composed by 400×80 elements with $r = 1$. The time step is $\Delta t = 0.004$, yielding a maximum advective Courant number $C_u \approx 0.26$ and a maximum acoustic Courant number $C \approx 2.5$. Figure 15 shows a comparison of the density between the initial and the final time. The initial density profile consists of two layers with different acceleration. Hence, a rotational motion is induced along the separating layer and a Kelvin-Helmholtz instability develops. This test case illustrates the non trivial interaction between large-scale acoustic waves and small-scale density fluctuations. Following the discussion in [38, 39] and in Section 3.2, we notice that the **x**-averaged mass and momentum balance for (48)-(49) read as follows:

$$\frac{\partial \bar{\rho}}{\partial t} = 0 \tag{131}$$

$$\frac{\partial \bar{\rho}\bar{\mathbf{u}}}{\partial t} + \nabla_{\boldsymbol{\xi}}\, p^{'} = 0. \tag{132}$$

Suppose now that two neighbouring mass elements characterized by densities ρ_1 and ρ_2, with $\rho_1 \neq \rho_2$ as in the present test case, are accelerated by a common large-scale acoustic pressure gradient. Since the time derivative of the momentum is the same for both mass elements, their velocities must differ by a factor of $\frac{\rho_2}{\rho_1}$. As a consequence of different accelerations, vorticity is generated. This phenomenon is also known as *baroclinic effect* and it is the result of mutual interaction between the quasi-incompressible small-scale and the large-scale acoustic flow.

Finally, we consider for this test case the SG-EOS (10). We take $\gamma = 4.4, \pi_\infty = 6.8 \times 10^{-3}$, and $q_\infty = 0$. The same initial conditions of the configuration with the ideal gas law are employed. The time step is $\Delta t = 2.5 \times 10^{-3}$, yielding a maximum acoustic Courant number $C \approx 3.5$ and a maximum advection Courant number $C_u \approx 0.23$. One can easily notice that the development of the Kelvin-Helmholtz instability depends on the EOS and on the fluid parameters (Figure 16).

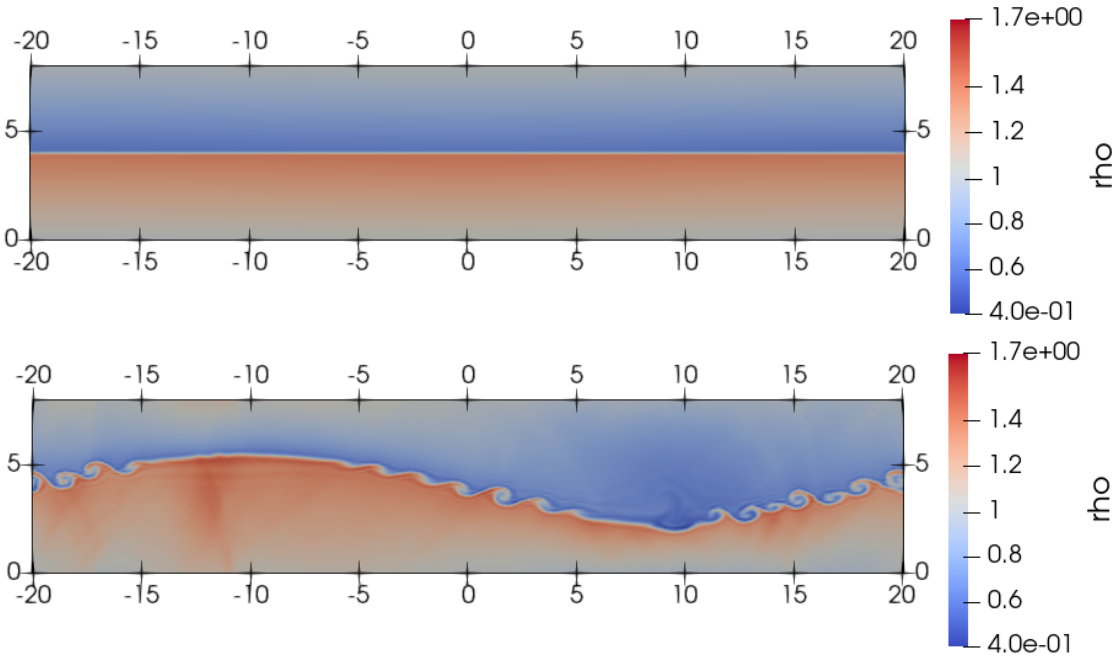

Figure 15: Baroclinic vorticity generation with the ideal gas law (9), contour plot of the density. Top: $t = 0$. Bottom: $t = T_f = 16$.

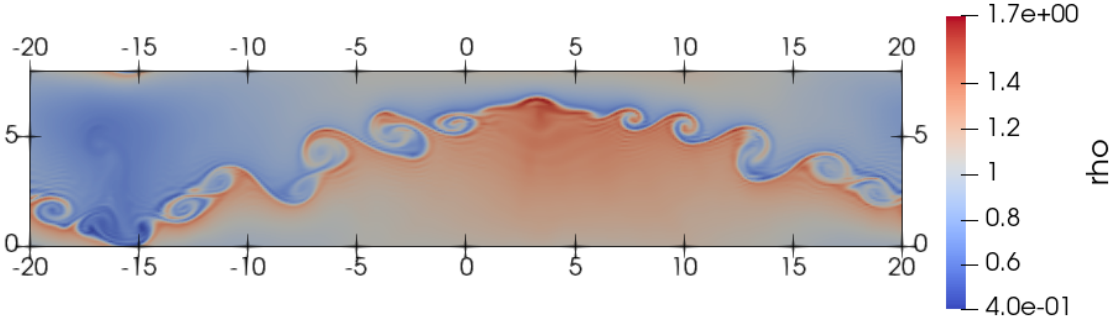

Figure 16: Baroclinic vorticity generation with the SG-EOS (10), contour plot of the density at $t = T_f = 16$.

6 Conclusions

We have presented the asymptotic-preserving (AP) analysis of a general IMEX approach for the time discretization of the compressible Euler equations. Based on the results of [12, 19], these approaches consider an implicit coupling between the momentum and the energy balance, while treating the density explicitly. The second order method proposed in [24], in combination with a Discontinuous Galerkin (DG) for the space discretization, has been employed for numerical simulations. The AP property of the proposed method is valid for a general equation of state as well as for two length scales models. A number of classical benchmarks for ideal gases and their non trivial extension for equations of state of real gases, in particular for the general cubic equation of state, validate the proposed method in the low Mach number regime and in

the limit of incompressible flows. Notice that, no operator splitting, flux splitting or relaxation techniques have been employed, unlike the approaches proposed e.g. in [1, 13, 14, 38, 44]. In future work, we aim to consider gravity effects, so as to perform an asymptotic analysis in the limit of low Froude numbers, and to consider an extension for two-phase flows.

A Eigenvalues of the implicit and explicit part

In this Appendix, we analyze the eigenvalues for the Euler equations (8). More specifically, we compute the eigenvalues for the two subsystems obtained considering the IMEX approach described in Section 3. For the sake of simplicity, we focus on 1D case, so that the equations can be written as follows:

$$\frac{\partial \rho}{\partial t} + \frac{\partial q}{\partial x} = 0 \tag{133}$$

$$\frac{\partial q}{\partial t} + \frac{\partial}{\partial x}\left(\frac{q^2}{\rho}\right) + \frac{1}{M^2}\frac{\partial p}{\partial x} = 0 \tag{134}$$

$$\frac{\partial \hat{E}}{\partial t} + \frac{\partial hq}{\partial x} + \frac{1}{2}M^2\frac{\partial}{\partial x}\left(\frac{q^3}{\rho^2}\right) = 0, \tag{135}$$

with $q = \rho u$ and $\hat{E} = \rho E$. Hence, considering the time discretization reported in Section 3, the system can be written in the following quasi-linear form:

$$\frac{\partial \tilde{\mathbf{W}}}{\partial t} + \tilde{\mathbf{A}}_I \frac{\partial \tilde{\mathbf{W}}}{\partial x} + \tilde{\mathbf{A}}_E \frac{\partial \tilde{\mathbf{W}}}{\partial x} = \mathbf{0}, \tag{136}$$

with

$$\tilde{\mathbf{W}} = \begin{bmatrix} \rho \\ q \\ \hat{E} \end{bmatrix} \tag{137}$$

$$\tilde{\mathbf{A}}_I = \begin{bmatrix} 0 & 0 & 0 \\ \frac{1}{M^2}\frac{\partial p}{\partial \rho} & \frac{1}{M^2}\frac{\partial p}{\partial q} & \frac{1}{M^2}\frac{\partial p}{\partial \hat{E}} \\ q\frac{\partial h}{\partial \rho} & q\frac{\partial h}{\partial q} + h & q\frac{\partial h}{\partial \hat{E}} \end{bmatrix} \tag{138}$$

$$\tilde{\mathbf{A}}_E = \begin{bmatrix} 0 & 1 & 0 \\ -u^2 & 2u & 0 \\ -M^2u^3 & \frac{3}{2}M^2u^2 & 0 \end{bmatrix}. \tag{139}$$

Here, $\tilde{\mathbf{A}}_I$ and $\tilde{\mathbf{A}}_E$ denote matrices related to the fluxes discretized implicitly and explicitly, respectively. After some manipulations (see [47]), we can rewrite (136) as follows:

$$\frac{\partial \mathbf{W}}{\partial t} + \mathbf{A}_I \frac{\partial \mathbf{W}}{\partial x} + \mathbf{A}_E \frac{\partial \mathbf{W}}{\partial x} = \mathbf{0}, \tag{140}$$

with

$$\mathbf{W} = \begin{bmatrix} \rho \\ u \\ p \end{bmatrix} \tag{141}$$

$$\mathbf{A}_I = \begin{bmatrix} 0 & 0 & 0 \\ 0 & 0 & \frac{1}{\rho M^2} \\ 0 & \frac{\frac{p}{\rho} - \rho \frac{\partial e}{\partial \rho}}{\frac{\partial e}{\partial p}} & u \end{bmatrix} \tag{142}$$

$$\mathbf{A}_E = \begin{bmatrix} u & \rho & 0 \\ 0 & u & 0 \\ 0 & 0 & 0 \end{bmatrix}. \tag{143}$$

The eigenvalues of $\mathbf{A}_I$ are

$$\frac{u}{2} - \sqrt{\frac{c^2}{M^2} + \frac{u^2}{4}} \qquad 0 \qquad \frac{u}{2} + \sqrt{\frac{c^2}{M^2} + \frac{u^2}{4}}, \tag{144}$$

while the eigenvalues of $\mathbf{A}_E$ are

$$0 \qquad u \qquad u. \tag{145}$$

Notice that, the eigenvalues of $\mathbf{A}_E$ are always real, meaning that the subsystem discretized explicitly is always hyperbolic, and no acoustic effect is taken into account.

References

[1] E. Abbate, A. Iollo, and G. Puppo. "An asymptotic-preserving all-speed scheme for fluid dynamics and nonlinear elasticity". *SIAM Journal on Scientific Computing* 5 (2019), A2850–A2879.

[2] D. Arndt et al. "The deal.II library, version 9.5". *Journal of Numerical Mathematics* 3 (2023), pp. 231–246.

[3] U.M. Ascher, S.J. Ruuth, and R.J. Spiteri. "Implicit-explicit Runge-Kutta methods for time-dependent partial differential equations". *Applied Numerical Mathematics* 25.2-3 (1997), pp. 151–167.

[4] W. Bangerth, R. Hartmann, and G. Kanschat. "deal.II: a general-purpose object-oriented finite element library". *ACM Transactions on Mathematical Software (TOMS)* (2007), pp. 24–51.

[5] L. Bonaventura and A. Della Rocca. "Unconditionally Strong Stability Preserving Extensions of the TR-BDF2 Method." *Journal of Scientific Computing* (2017), pp. 859–895.

[6] S. Boscarino, F. Filbet, and G. Russo. "High order semi-implicit schemes for time dependent partial differential equations". *Journal of Scientific Computing* 68 (2016), pp. 975–1001.

[7] W. Boscheri et al. “A second order all Mach number IMEX finite volume solver for the three dimensional Euler equations”. *Journal of Computational Physics* (2020), p. 109486.

[8] P. Bruel et al. “A low Mach correction able to deal with low Mach acoustics”. *Journal of Computational Physics* (2019), pp. 723–759.

[9] E. Buckingham. “On physically similar systems; illustrations of the use of dimensional equations”. *Physical review* 4 (1914), p. 345.

[10] S. Busto et al. “A semi-implicit hybrid finite volume/finite element scheme for all Mach number flows on staggered unstructured meshes”. *Applied Mathematics and Computation* (2021), p. 126117.

[11] J. Butcher. *Numerical Methods for Ordinary Differential Equations*. 2nd ed. Wiley, 2008.

[12] V. Casulli and D. Greenspan. “Pressure method for the numerical solution of transient, compressible fluid flows”. *International Journal for Numerical Methods in Fluids* (1984), pp. 1001–1012.

[13] C. Chalons, M. Girardin, and S. Kokh. “Large time step and asymptotic preserving numerical schemes for the gas dynamics equations with source terms”. *SIAM Journal on Scientific Computing* 6 (2013), A2874–A2902.

[14] C. Chalons, M. Girardin, and S. Kokh. “An all-regime Lagrange-Projection like scheme for the gas dynamics equations on unstructured meshes”. *Communications in Computational Physics* 1 (2016), pp. 188–233.

[15] A.J. Chorin. “A numerical method for solving incompressible viscous flow problems”. *Journal of Computational Physics* 2 (1967), pp. 12–26.

[16] F. Cordier, P. Degond, and A. Kumbaro. “An asymptotic-preserving all-speed scheme for the Euler and Navier-Stokes equations”. *Journal of Computational Physics* 17 (2012), pp. 5685–5704.

[17] G. Dimarco, R. Loubère, and M.-H. Vignal. “Study of a new asymptotic preserving scheme for the Euler system in the low Mach number limit”. *SIAM journal on Scientific Computing* 5 (2017), A2099–A2128.

[18] G. Dimarco et al. “Second-order implicit-explicit total variation diminishing schemes for the Euler system in the low Mach regime”. *Journal of Computational Physics* (2018), pp. 178–201.

[19] M. Dumbser and V. Casulli. “A conservative, weakly nonlinear semi-implicit finite volume scheme for the compressible Navier-Stokes equations with general equation of state”. *Applied Mathematics and Computation* (2016), pp. 479–497.

[20] M. Dumbser and R. Loubère. “A simple robust and accurate a posteriori sub-cell finite volume limiter for the discontinuous Galerkin method on unstructured meshes”. *Journal of Computational Physics* (2016), pp. 163–199.

[21] E. Feireisl et al. “On singular limits arising in the scale analysis of stratified fluid flows”. *Mathematical Models and Methods in Applied Sciences* 03 (2016), pp. 419–443.

[22] K.J. Geratz. “Erweiterung eines Godunov-Typ-Verfahrens für mehrdimensionale kompressible Strömungen auf die Fälle kleiner und verschwindender Machzahl”. PhD thesis. RWTH Aachen, 1998.

[23] F.X. Giraldo. *An Introduction to Element-Based Galerkin Methods on Tensor-Product Bases*. Springer Nature, 2020.

[24] F.X. Giraldo, J.F. Kelly, and E.M. Constantinescu. “Implicit-Explicit Formulations Of A Three-Dimensional Nonhydrostatic Unified Model Of The Atmosphere (NUMA)”. *SIAM Journal of Scientific Computing* (2013), pp. 1162–1194.

[25] S. Gottlieb, C. W. Shu, and E. Tadmor. “Strong stability-preserving high-order time discretization methods”. *SIAM Review* (2001), pp. 89–112.

[26] N. Grenier, J.-P. Vila, and P. Villedieu. “An accurate low-Mach scheme for a compressible two-fluid model applied to free-surface flows”. *Journal of Computational Physics* (2013), pp. 1–19.

[27] P.M. Gresho. “On the theory of semi-implicit projection methods for viscous incompressible flow and its implementation via a finite element method that also introduces a nearly consistent mass matrix. Part 1: Theory”. *International Journal for Numerical Methods in Fluids* 5 (1990), pp. 587–620.

[28] J. Haack, S. Jin, and J.-G. Liu. “An all-speed asymptotic-preserving method for the isentropic Euler and Navier-Stokes equations”. *Communications in Computational Physics* 4 (2012), pp. 955–980.

[29] N. Happenhofer et al. “A low Mach number solver: enhancing stability and applicability”. *ArXiv e-prints* (2011).

[30] F.H. Harlow and A.A. Amsden. “Numerical calculation of almost incompressible flow”. *Journal of Computational Physics* 1 (1968), pp. 80–93.

[31] F.H. Harlow and A.A. Amsden. “A numerical fluid dynamics calculation method for all flow speeds”. *Journal of Computational Physics* 8.2 (1971), pp. 197–213.

[32] A. Hennink, M. Tiberga, and D. Lathouwers. “A pressure-based solver for low-Mach number flow using a discontinuous Galerkin method”. *Journal of Computational Physics* 425 (2021), p. 109877.

[33] R. Herbin, W. Kheriji, and J.-C. Latché. “On some implicit and semi-implicit staggered schemes for the shallow water and Euler equations”. *ESAIM: Mathematical Modelling and Numerical Analysis* 6 (2014), pp. 1807–1857.

[34] R. Herbin, J.-C. Latché, and K. Saleh. “Low Mach number limit of some staggered schemes for compressible barotropic flows”. *Mathematics of Computation* 329 (2021), pp. 1039–1087.

[35] M.E. Hosea and L.F. Shampine. “Analysis and implementation of TR-BDF2.” *Applied Numerical Mathematics* (1996), pp. 21–37.

[36] C.A. Kennedy and M.H. Carpenter. “Additive Runge-Kutta schemes for convection-diffusion-reaction equations”. *Applied Numerical Mathematics* (2003), pp. 139–181.

[37] S. Klainerman and A. Majda. “Singular limits of quasilinear hyperbolic systems with large parameters and the incompressible limit of compressible fluids”. *Communications on pure and applied Mathematics* 4 (1981), pp. 481–524.

[38] R. Klein. “Semi-implicit extension of a Godunov-type scheme based on low Mach number asymptotics I: One-dimensional flow”. *Journal of Computational Physics* 2 (1995), pp. 213–237.

[39] R. Klein. “Numerical modelling of high speed and low speed combustion”. *Nonlinear PDE’s in Condensed Matter and Reactive Flows*. Springer, 2002, pp. 189–226.

[40] R. Klein et al. “Asymptotic adaptive methods for multi-scale problems in fluid mechanics”. *Journal of Engineering Mathematics* (2001), pp. 261–343.

[41] V. Kučera et al. “Asymptotic properties of a class of linearly implicit schemes for weakly compressible Euler equations”. *Numerische Mathematik* (2022), pp. 1–25.

[42] O. Le Métayer and R. Saurel. “The Noble-Abel Stiffened-Gas equation of state”. *Physics of Fluids* (Apr. 2016), p. 046102.

[43] R. Liska and B. Wendroff. “Comparison of several difference schemes on 1D and 2D test problems for the Euler equations”. *SIAM Journal on Scientific Computing* 3 (2003), pp. 995–1017.

[44] S. Noelle et al. “A weakly asymptotic preserving low Mach number scheme for the Euler equations of gas dynamics”. *SIAM Journal on Scientific Computing* 6 (2014), B989–B1024.

[45] G. Orlando. “A filtering monotonization approach for DG discretizations of hyperbolic problems”. *Computers & Mathematics with Applications* (2023), pp. 113–125.

[46] G. Orlando. “Modelling and simulations of two-phase flows including geometric variables”. `http://hdl.handle.net/10589/198599`. PhD thesis. Politecnico di Milano, 2023.

[47] G. Orlando, P.F. Barbante, and L. Bonaventura. “An efficient IMEX-DG solver for the compressible Navier-Stokes equations for non-ideal gases”. *Journal of Computational Physics* (2022), p. 111653.

[48] G. Orlando, T. Benacchio, and L. Bonaventura. “An IMEX-DG solver for atmospheric dynamics simulations with adaptive mesh refinement”. *Journal of Computational and Applied Mathematics* (2023), p. 115124.

[49] G. Orlando et al. “An efficient and accurate implicit DG solver for the incompressible Navier-Stokes equations”. *International Journal for Numerical Methods in Fluids* (2022), pp. 1484–1516.

[50] V. Rusanov. “The calculation of the interaction of non-stationary shock waves and obstacles”. *USSR Computational Mathematics and Mathematical Physics* (1962), pp. 304–320.

[51] J. Steppeler et al. “Review of numerical methods for nonhydrostatic weather prediction models.” *Meteorology and Atmospheric Physics* (2003), pp. 287–301.

[52] I Suliciu. “On modelling phase transitions by means of rate-type constitutive equations. Shock wave structure”. *International Journal of Engineering Science* 8 (1990), pp. 829–841.

[53] M. Tavelli and M. Dumbser. “A pressure-based semi-implicit space-time discontinuous Galerkin method on staggered unstructured meshes for the solution of the compressible Navier-Stokes equations at all Mach numbers”. *Journal of Computational Physics* (2017), pp. 341–376.

[54] R. Temam. “Sur l’approximation de la solution des équations de Navier-Stokes par la méthode des pas fractionnaires (II)”. *Archive for Rational Mechanics and Analysis* (1969), pp. 377–385.

[55] N. Therme and C. Zaza. “Comparison of cell-centered an staggered pressure-correction schemes for all-Mach flows”. *Finite Volumes for Complex Applications VII - Elliptic, Parabolic and Hyperbolic*. J. Fuhrmann, M. Ohlberger, and C. Rohde, editors, 2014, pp. 975–983.

[56] A. Thomann et al. “An all speed second order IMEX relaxation scheme for the Euler equations”. *Communications in Computational Physics* (2019), pp. 591–620.

[57] J. Vidal. *Thermodynamics: Applications to chemical engineering and petroleum industry*. Editions Technip, 2001.